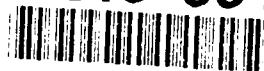


AD-A246 664



2

ONR Final Technical Report

Scanning Tunneling Microscope Studies of Surface Defects

Contract N00014-90-J-1003

1 October 1989 - 30 September 1991

Prof. Thomas Engel
Kevin E. Johnson
Department of Chemistry BG-10
University of Washington
Seattle, Washington 98195



17 December 1991

This document has been approved
for release and sale; its
contents are unclassified.

92-04986



92 2 26 002

~~91 1227 108~~

1. Project Overview

The goals of this study have been to design and construct a scanning tunneling microscope to study the energetics and interaction of defects on single crystal surfaces in ultrahigh vacuum. A number of these goals have been met. Among them are

- a state-of-the-art STM for surface studies is now operational. It includes a load lock system, a sample preparation chamber, and a microscope chamber. Using the load lock, samples can quickly be introduced into the system without impacting the vacuum conditions. In the analysis chamber, the sample can be heated, cleaned using chemical methods and noble gas sputtering, and analyzed with LEED and AES. After preparation, the sample can be transferred through a UHV isolation valve to the STM chamber. Any of the STM chamber, analysis chamber, or load lock system can be brought up to air without impacting UHV conditions in the other parts of the system. Schematic drawings are included in the Appendix to this report.

A second UHV STM system for atomic resolution studies of buried interfaces has been constructed and is now operational. Samples can be introduced through a loadlock system and are cleaved in UHV. After cleavage the sample is examined with the STM. A projection microscope using a HeNe laser is used to locate the tip relative to the wafer surface. The microscope gives a magnification of 150x so that the fine screw motion for adjusting the tip height relative to the solid-solid interface and the 5 micron range of the piezo should make it relatively easy to locate the interface. To date the system has been tested with Si(100) wafers which have been cleaved to give a Si(111) surface with a (2x1) reconstruction. Atomic resolution was obtained.

- A detailed study of the inhomogeneous thermal decomposition of ultrathin layers of oxide on Si(100) has been examined. This is particularly relevant to questions such as monolayer peeling. A particularly important result of these experiments is that even for only one monolayer of oxygen, the underlying substrate undergoes very substantial rearrangement upon thermal removal of the oxide. These experiments are described in detail in the technical part of this report. This work will be submitted for publication in the next 2 months.

2. Work in Progress

Since funding for this project has expired, planning for future experiments has continued. The multipurpose STM system is equipped with a pulsed Nd YAG laser to create high temperature excitations on surfaces. By the very rapid cooling inherent in this nanosecond pulse technique, it should be possible to freeze in high temperature surface configurations and to image

them subsequently at 300K. This should give important insight into the energetics of thermal excitations on surfaces. Our initial experiments have been carried out on Ag(115) and Ag(117). However, these surfaces already exhibit significant disorder and motion at 300K. We plan to investigate Si(100) and Si(111) first before proceeding with more densely packed metal surfaces. This will require frequency doubling of the laser to overcome the Si band gap.

On the cleavage STM, we plan to look at the atomic level structure at the Ni-GaAs interface. The focus will be on gaining a better understanding of Fermi level pinning in this system. At present this work is being planned together with Dr. Scott Chambers of Boeing.

3. **Personnel**

The following individuals have been supported by this project in the past 3 years.

Kevin Johnson has completed his PhD. thesis with work obtained in this project. He will take a postdoctoral research associate position at the IBM Almaden Laboratory in January 1992.

Peter Wu was a postdoctoral research associate supported by the project. He is now a postdoctoral research associate at RPI.

4. **Technical Results**

Structural Studies of the Decomposition and Desorption of Ultra-thin Oxide Layers on Si(100).

For surface modifying chemical reactions, STM offers a means to measure — in real space — the evolution of surface structure as the reaction proceeds. Detailed in this section is the first application of this method to study the mechanism of a decomposition reaction. The spatially inhomogeneous oxide decomposition and desorption reaction of 1 to 0.3 monolayer oxygen coverages from a silicon (100) surface was studied using the UHV STM described above.

In the initial stages of oxide removal, void formation is imaged and the distributed void density, shape, and area are quantified as a function of the fraction of removed oxide. Using measured void size distributions at total desorption levels of 13% and below — where voids have not yet begun to coalesce — the evolution of void sizes during this initial desorption stage can be quantitatively evaluated. Two void growth mechanisms are proposed and two models derived for the desorption reaction: the first is a mechanism where the silicon source for the desorption of SiO is removed at the boundary between remaining oxide and clean silicon, and the second mechanism

supposes that the silicon which is removed must diffuse from adjacent oxide free surface area to the oxide void perimeter. By calculating the growth evolution as governed by each model from an initial void area density distribution similar to that measured, we show that the measured evolution is consistent with the second mechanism where the desorbing silicon atom source is from clean surface within the void perimeters.

Images taken of the surface after desorption was nearly complete, showed unexpected roughening and pitting of the silicon surface. Image analysis of these chemically roughened surfaces attests to an increased edge density of by factor of up to 20 when compared to the annealed clean Si(100) surface. STM images of the surface after complete removal of the oxide layer exhibit metastable surface reconstructions with decreased surface atom density. Along with the consistently observed '(2×n)' reconstruction, domains of a Si(100)-c(4×4) reconstruction were imaged, for the first time with STM. The c(4×4) atomic structure is modeled and a mechanism for its formation is proposed.

This study demonstrates the capacity for STM to uniquely quantify surface structural changes which result from inhomogeneous modification of a surface by chemical reaction.

A. Background

Phenomena which are spatially inhomogeneous and have atomic length scale interactions are suitable and interesting candidates for study using STM. The broad class of epitaxy, including metal¹ and semiconductor² materials on semiconductor substrates and metal on metal systems,³ have been previously examined using STM. Another class of surface phenomena which should be suitable for examination with STM would be heterogeneous reaction and catalysis at a surface with preexisting spatial heterogeneity. Initial stages of chemisorption on silicon of ammonia⁴ and oxygen^{5,6} have been reported. These reactions show spatial selectivity but do not significantly alter long range surface structure until higher levels of adsorption are reached. In this study surface structure is imaged for a spatially heterogeneous chemical reaction which modifies the surface over microscopic to mesoscopic dimensions.

The technologically relevant and scientifically interesting decomposition and desorption reaction of thin silicon oxide layers grown on silicon surfaces has recently been studied using microscopic and chemical techniques. Rubloff, Liehr, and coworkers,⁷ in the first studies of this system, showed that at elevated temperatures the desorption reaction of oxide films with thickness of 100 to 1000Å produced exclusively a SiO gas phase product. They also showed, using electron microscopy techniques, that the reaction

proceeded spatially inhomogeneously, producing open voids within the oxide layer which exposed the underlying silicon substrate. The void diameters, which they measured in a range of 2 - 100 μm , were shown to grow with increasing desorption time or temperature. Linear growth rate for void diameters was observed for constant temperature desorption, implying a rate limiting step for the desorption reaction which depends on the void perimeter. In another microscopic study, Kobayashi and Sugii⁸ used STM to measure the void formation in 12Å thick oxide layers which were grown outside of vacuum by aqueous chemical oxidation, and partially removed by thermal desorption in vacuum. The resulting voids were imaged in air. They report average void diameters of 1.0×10^3 to 2.0×10^3 Å, also increasing in size with increasing total desorption.

Previous studies in our group have used chemical methods to probe the decomposition and desorption reaction inhomogeneity by thermal desorption and mass spectrometry (TDS). The peak desorption temperature for an oxide layer was shown to vary with *local* coverage. This provides a means to measure with a single TDS experiment the fractional surface area with different local coverages. In a partial desorption and readsorption study, the clean surface area of voids formed by partial desorption of an initial oxide layer was titrated using a lower oxygen exposure readsorption onto the clean silicon within the formed voids. The total void area was subsequently quantified by TDS measurement, where the initial and readsorbed oxide desorbed at distinct temperatures. The results showed that 4-10 monolayers (ML) oxygen coverages did not thin locally as desorption proceeded and that the fractional area of clean silicon exposed on the surface quantitatively equaled the fraction of desorbed initial oxide.⁹ Additional experiments concluded that the inhomogeneity in desorption extended to coverages as low as 0.3ML.¹⁰ Isotopic labeling experiments indicate that oxygen on the surface is not mobile during desorption and that for a 1ML coverage the oxygen which is first adsorbed is the last desorbed as SiO.

Previous STM studies of oxygen chemisorption on Si(111),⁵ and more recently on Si(100),⁶ have focused on structural aspects of the initial stages of adsorption. At very low coverages the preferential sites for initial adsorption have been identified. STM experiments have provided structural as well as spectroscopic evidence for two different adsorption bonding configurations, both of which involve insertion of an oxygen atom into the silicon-silicon backbond.

Oxide layers formed at elevated temperatures with thickness of 4 ML and above form SiO₂. As the desorption product is SiO, an additional silicon source is required for the reaction to proceed. The source of this additional silicon is thought to be from within the voids formed in the oxide layer. In contrast the ultra-thin oxides we examined using STM were formed by oxygen exposure at room temperature with coverage 0.3 to 1 ML. Such thin layers

are not expected to be fully formed SiO_2 , and in any case should require no more than a single surface layer of silicon be removed in the desorption reaction. (1 ML is defined here as one oxygen atom per silicon atom at the surface.)

That the desorption of ultra-thin oxide layers still proceeds inhomogeneously, and leaves the surface in a roughened state, indicates either energetic inhomogeneity of the bound oxide species on the surface, local heterogeneous kinetic barriers to desorption, or a spatially inhomogeneous reaction mechanism. Real space measurement of the microscopic surface structure at intermediate stages of partial desorption can provide a better picture of the microscopic origins of the reaction inhomogeneity.

B. Experimental Procedures

All measurements and sample preparation were performed in the dual chamber UHV STM system detailed above and shown in the appendix. All images shown were taken using constant current topography STM. In order to achieve low noise and reproducible images a set of optimized tunneling parameters was used. For clean silicon surfaces a tunneling voltage of $V_{\text{tip}} = +2\text{V}$, and a tunneling current of $i_{\text{tunnel}} = 1\text{nA}$ provided the best results. Imaging on samples where the majority of the surface was oxide covered required an increase in the tunneling voltage to $V_{\text{tip}} = +4\text{V}$, which stabilized the tunneling current and produced structurally resolved images. While constant current topography does not provide an ideal contrast mechanism for differentiating oxide from clean silicon, STM images consistently show the restored $\text{Si}(100)\text{-(}2\times 1\text{)}$ reconstruction for clean areas within desorbed voids, and adjacent disordered surface regions which are interpreted as remaining oxide.

All oxidation was performed with the sample at room temperature. The clean and annealed silicon surface was exposed to varying amounts of O_2 via the gas doser. Coverages were measured by AES and calibrated to the $\frac{1}{2}$ ML saturation of water adsorption on the $\text{Si}(100)$ surface.¹¹ Figure 1 shows the saturation of the AES O_{KLL} intensity for increasing oxygen exposure. The figure plots fractional AES intensity, corrected to atomic sensitivity factors, against exposure (the exposure scale is here not corrected for the enhancement factor for the sample doser). The O_2 exposure was performed in conditions which minimized concurrent sample contamination. The small carbon signal, $<0.5\%$, detected by AES is the result of contamination during the AES measurement, not from O_2 exposure. The fact that the oxygen adsorption for 1ML saturates rapidly with only very slow adsorption at greater exposures, allowed for reproducible 1ML oxygen coverages. For the initial coverages of less than a monolayer, small dosage errors combined with

the rapid initial adsorption of oxygen necessitated individual AES measurements for each exposure.

Oxide layers were partially desorbed by temperature controlled heating of the oxidized sample. Initially the sample temperature was stabilized at $\approx 800\text{K}$, a point below the desorption temperature. For desorption, the sample temperature was ramped over 1 minute to a predetermined point, then held constant. At this predetermined temperature the extent of desorption could be controlled by time. After partial desorption, the heating was terminated and the sample allowed to cool radiatively. For a 1 ML initial coverage the controlled desorption temperature was $\approx 1000\text{K}$ and for the 0.3 ML initial coverage a temperature 15° lower was used. At these temperatures time increments of 15 seconds would only partially remove the oxide layers.

Complete desorption was accomplished simply by cumulative heating to the same desorption temperatures. Additionally the samples were heated to 1075K after complete desorption to observe the annealing of step edges. Only after extended heating to higher temperatures of 1525K was the sample surface completely restored to the initial low defect density state observed with STM prior to oxidation. At these temperatures it is likely the restoration of the initial surface involves more than the diffusion of surface silicon atoms, as the sublimation rate is appreciable. (The sublimation rate estimated from vapor pressure at 1525K is 3×10^{-2} ML per second.)

This section includes STM images of the Si(100) surface at each stage in this process: clean, oxidized with 1.0 and 0.3 ML oxygen coverages, partially desorbed at different levels desorption, and after complete removal of the oxide.

C. Experimental Results

Shown in figure 2 are STM images of clean Si(100)-(2 \times 1). The atomic structure of this surface was discussed in detail in the preceding chapter. These images are typical of the initial surfaces used for the oxide desorption studies. From these images various aspects of the clean surface structural order and disorder can be quantified. First, vacancy densities of less than 4% are routinely achieved by the surface preparation procedure; from simple counting of these vacancy defects, the surface density is measured to be roughly 3.1×10^{-4} per \AA^2 . Second, calculated from the average measured terrace width in long range images such as figure 2(a), the measured local misorientation from the [100] direction for samples used for this study was between 0.06° and 0.1° . The majority of the samples imaged had an orientation tilted in the $[01\bar{1}]$ direction giving the alternating smooth and jagged step edges described previously.

In order to compare the roughness of the initial silicon surfaces to that of the surface after partial and complete desorption of oxide layers, we quantify the edge structure in STM images in two ways. First, for each type of step edge, the ratio of the measured length of a given edge boundary to the end to end straight distance traversed by that step edge on the surface is calculated. Note that the length measured for the edge boundary does depend somewhat on the resolution of the image used, and to make a good estimate of the straight length a lower resolution, long range image is preferable. To avoid inconsistencies all such measurements were taken with images of similar size and resolution. For well annealed clean surfaces the calculated average ratio for smooth type edges is 1.0 (+0.4), and for jagged type edges 1.3 (± 0.2). Additionally, the total length of step edge in one image is measured and normalized to the image area, yielding a step edge density, which for annealed surfaces measured here is 1.4×10^{-3} Å length per Å² area. This quantity can be compared to the step edge density expected should the surface have only perfectly straight step edges; for surfaces, with a vicinal orientation of 0.08°, this value — which is simply the inverse of the mean terrace width — would be 1.03×10^{-3} Å length per Å² area. Table 1 is included as a compilation of the roughness measurements made throughout this desorption study.

After room temperature exposure to molecular oxygen producing oxygen coverages of 0.3 ML to 1 ML, STM images of the surface show no evidence of the (2×1) reconstruction. The images show homogeneous adsorption but local disorder on the previously flat terraces. Because constant current STM topography can not directly separate atomic structure from electronic effects, it is not possible to quantify the atomic scale structural effects of oxidation at these coverages. However, figure 3 demonstrates that the long range terrace and step structure of the clean surface remains unchanged. Imaged at higher resolution in figure 4 are regions of equal size taken for 1 ML and 0.3 ML oxygen coverages; neither shows aspects of the order of the underlying Si(100) terrace, though a step edge appears in both. There is, however, a qualitative difference in the appearance of these two images. The higher coverage surface appears to have a higher density of small granular features.

In the initial stage of decomposition and desorption, it is possible to image the voids formed in the oxide layer. This initial stage is defined here as desorption up to the point where the voids begin to significantly grow together. Figure 5 is a 4000Å × 4000Å image of the surface after approximately 7.8% of an initial 1 ML coverage has been removed. In this and all subsequent images of voids, the estimated fraction of desorbed oxide is calculated from the measured sum of all void areas in the STM images. From images at this stage of desorption, it can be seen that the terrace and step structure of the initial surface is still preserved, and that the formation of voids is spatially homogeneous with no location preference on the terraces.

Figure 6 shows three images taken at equal size and resolution as increasing fractions of an initial 1ML oxygen coverage are removed. At 13% oxide removal shown in figure 6 (c), it is possible, at higher resolution, to image clean Si(100) surface with the restored (2×1) reconstruction within the larger voids. Also in figure 6 (c) it is apparent that the general shape of the voids is not round; in fact the edges of the larger voids appear to be parallel with the dimer row directions of the underlying silicon. Both total void area and number of voids are quantified for these three images. The first quantity is a measure of extent of desorption, the second a measure of surface void density, which for these images remains constant or decreases slightly as the voids begin to grow together. For a one monolayer initial coverage the measured void density is $1.0 \times 10^{-4} (\pm 0.3 \times 10^{-4})$ per \AA^2 , which corresponds to a 1.5×10^{-3} ML surface density. (This value is three orders of magnitude greater than that reported for 12Å thick oxides in a previous STM study⁸ and eight orders of magnitude greater than that reported for a 500Å thick oxide measured by SEM.⁷) It is also possible to quantify the distribution of void density as a function of void area, providing a means of characterizing the evolution of void areas as desorption proceeds in this initial stage. In the following section we will discuss in detail these density distributions of void areas measured from the images shown in figure 6.

At later stages of desorption the terrace and step structure of the exposed Si(100) surface is significantly altered. Figure 7 illustrates the surface structure after >50% removal of an initial coverage of 0.3 ML. Likewise figure 8 illustrates the surface structure after removal of an initial full monolayer coverage to ≈12% remaining oxide. At this stage of the reaction the disordered regions in each image are quantified as a measure of the remaining oxide coverage. The roughened appearance of both images is contrary to the expectation that desorption removes only a single layer of Si from the surface.

After removal from the initial sub-monolayer oxygen coverage, the surface step structure can still be seen in figure 7(a), however the terraces are locally roughened. In figure 7(b) a step edge runs diagonally through the image from upper left to lower right. It is the smooth type step with dimer rows parallel to the step edge. The two terrace levels shown here consist primarily of the dimer rows at the terrace level with single layer deep pits and on top islands of (2×1) patches. Remaining disordered regions are the undesorbed oxide. The on-top silicon islands appear as individual dimer rows, similar to the islands observed with STM after silicon epitaxy on Si(100).¹²

In figure 8(a) the surface has been so roughened that locally the terrace and step structure of the surface is no longer apparent. Macroscopic surface slope, or miscut, must be maintained, but at the length scales of an STM image the surface has been roughened to such a degree that the local height variations obscure the previously observed step structure. An image the size

of figure 3(a) would, on a clean ordered surface, encompass one to three step edges. What is observed instead is local pitting of the surface to depths up to 5 layers deep. Because of the pitting, the edge density on the surface is greatly increased with respect to the clean annealed surface; the measured edge density for the surface in this state is 3.0×10^{-2} Å length per Å² area, an increase by a factor of 20 (see table 1). This increased edge density is a potential source of diffusing silicon at the sample temperatures used during decomposition and desorption. At higher resolution in figure 8(b) a pit is shown at the right edge of the image. Local regions of disorder, interpreted as remaining oxide, appear exclusively on the upper terrace level of remaining silicon, with surrounding clean silicon at the same level. These images contradict a simple mechanism where SiO desorbs from the surface by removal of the top layer of silicon with which the adsorbed oxygen has reacted.

By quantifying the apparent volume of removed silicon from layers below the top remaining level in images taken at this later stage of partial desorption, the amount of silicon removed from the surface can be estimated. This value is a factor 1.9 to 2.5 greater than the fraction of removed oxide! The surfaces appear to show removal of more silicon than can be accounted for with SiO desorption alone. Discussion of this apparent discrepancy will be deferred to the following section.

Although the silicon surfaces imaged in figures 7 and 8 have roughly equivalent amounts of remaining oxide, there is a considerable difference in the local roughening. While decomposition of the full monolayer coverage removes a greater amount of silicon from the surface, it would require no more than a single layer of silicon to produce the SiO desorption product. The additional pitting, shown in figure 8, can not therefore be explained by a simple greater requirement of silicon atoms. In the case of the partial initial oxygen coverage the apparent movement of silicon to sites on top of an existing layer points to the presence of some mechanism which allows for the growth of silicon islands during oxide removal. Silicon diffusion is expected to be facile at the desorption temperatures used for these experiments, although a temperature 15° lower was used for desorption of the 0.3 ML oxide. Further explanation of the structural differences resulting from the removal of partial and full monolayer oxides requires first a discussion of the possible reaction mechanisms, which appears in the following section.

The complete removal of monolayer and sub-monolayer oxygen coverages yields surfaces with roughened step edges but with vertical roughening (i.e. multi-level pitting) now absent. The surface after complete removal of 0.3ML is shown in figure 9. The image shows a terrace into which monolayer deep pits have been formed, and onto which monolayer high islands have grown. A step edge density of 1.7×10^{-2} Å length per Å² area is measured for this surface, an increase by a factor of 12 from the clean surface. (The roughening of individual edges can not be assessed for this surface

because most of the edges in the images are perimeters of pits or islands, and as continuous edges can not be assigned a single edge type or travel length.)

After removal of the full monolayer coverage, the surface shown in figure 10 also appears roughened, but with no remaining pitting in the surface. The transition from the previous state of a highly roughened surface with a small amount of remaining oxide to the clean surface is analogous to the coarsening and annealing of surfaces after homoepitaxy.¹³ But here the annealing processes differs from homoepitaxy, in that for epitaxy only islands are present, whereas surface roughening from both islands and pits results from the oxide desorption.

From figure 10(a) it is apparent that terrace edges are continuous across the image and only occasional islands on top of terraces are seen. Using the image of figure 10(a), and others of the surface after full monolayer oxide removal, the step edge roughness is quantified as previously described for the clean surface: smooth type edges have a measured length roughness of ≈ 1.3 , and jagged type edges have roughened to a ratio of ≈ 2.6 . By this measure the roughness ratios of smooth and jagged type step edges has increased by a factor of 1.25 and 2.0 respectively. Edge density measured on this surface yields 3.7×10^{-3} Å length per Å² area, increased by a factor of 2.6 from the clean surface.

Besides the mesoscopic roughening of steps and terraces, at the shorter length scales of figures 9 and 10(b) it is apparent that the local structure of the (2×1) reconstruction has been altered. Shown in figure 11(a) is a high resolution image of the Si(100) surface after complete removal of a full monolayer oxide. In every case after partial and complete removal of an oxide layer, the observed Si(100)-(2×1) structure has been altered by the addition of chains of missing dimers perpendicular to the dimer row direction. These vacancy chains appear with regular separations in the direction parallel to the dimer rows. This so called (2×n) reconstruction, where $6 \leq n \leq 10$, is frequently observed on the Si(100)-(2×1) surface using both LEED¹⁴ and STM.¹⁵ It is always observed in presence of nickel contamination of the sample.¹⁶ Metallic contamination is not the cause of the reconstruction in this case: first no evidence of nickel is observed in the Auger spectra to less than 0.2% surface atomic concentrations, and second the vacancy chains from oxide desorption are removed after high temperature heating of the sample, which is not the case when the (2×n) results from nickel or other metallic contamination. With the exception noted below this vacancy chain reconstruction covers the entire exposed silicon surface with a roughly 17% vacancy density. The chain lengths average 60Å, the width equivalent to two missing dimers, and the measured depth 0.3Å.

For some surfaces after desorption, STM images exhibit a new — previously unreported by STM — Si(100) reconstruction shown in figures 10(b) and 11(b). Domains of the new reconstruction appear within terraces and at the terminating edge of terraces. The domains have a mean area of $5 \times 10^4 (\pm 3 \times 10^4) \text{ \AA}^2$, and a roughly elliptical shape with long axis $2.8 (\pm 1.5)$ times the short axis, oriented parallel to the dimer rows. The primary structure is a $c(4 \times 4)$ unit cell outlined in figure 12(a). The basic periodicity between dimer rows is maintained, however the rows appear incomplete. The intra-row repeat distance parallel to the dimer rows is twice the distance between dimer rows on the underlying layer. The repeat unit within a row consists of either a maxima at the level of the complete top layer dimer or a hole of measured depth greater than the single layer step height, followed by two intermediate maxima. The presence or absence of the highest maxima induces disorder in the reconstructed domains, although the holes appear to align in diagonal chains. The inter-row periodicity is shifted at adjacent rows by the distance equal to a single underlying dimer row; this gives rise to the '4×' periodicity perpendicular to the dimer rows and the centered element of the $c(4 \times 4)$ structure. Missing symmetry operations for this complex $c(4 \times 4)$ unit cell are four fold rotation and diagonal reflection. The two dimensional point group is therefore $2mm$. Alignment of the structural elements of this reconstruction with adjacent lower terraces shows the highest maxima — or hole — in this structure always corresponds to a location on top of every other underlying dimer row, and the two intermediate maxima always lie on either side of the alternate underlying dimer rows. When present these $c(4 \times 4)$ domains are observed on approximately 15% of the surface. A detailed description of the interpretation of this reconstruction is in the following section on image interpretation.

Both the $(2 \times n)$ and $c(4 \times 4)$ reconstructions result in a decreased surface atom density. For the $(2 \times n)$ reconstruction the surface atom density is 83% of that on a 'perfect' Si(100) surface. For the $c(4 \times 4)$ reconstruction, if one interprets the maxima — both highest and intermediate — as dimers, the atom density within the domains of $c(4 \times 4)$ is 78% of a perfect Si(100)- (2×1) , or 82% atom density for the observed 15% : 85% mixture of $(2 \times n)$: $c(4 \times 4)$ domains.

If, after complete removal of oxide, the sample is annealed to temperatures 75° higher than the desorption and decomposition temperatures, the terrace edge roughening is removed and $c(4 \times 4)$ domains are likewise no longer observed. However the vacancy chains of the $(2 \times n)$ reconstruction remain until the surface has been heated to temperatures of 1525K for a total time of greater than 1 minute.

D. Discussion

The images presented in the previous section can be evaluated on three levels. The first is simple identification of structural features. The preceding descriptions constitute this first level of evaluation. The second level is the quantitative analysis (i.e. area, density, shape, etc.) of features observed in the STM images. For this level of description we use the term image analysis. Further explanation of the processes from which the observed surface morphology originates, constitutes an additional interpretative level, which we shall call image interpretation.

Image Analysis

In order to quantify the structural features of the images from this study, an image processing and analysis program¹⁷ was used. In addition to standard STM height profile interpretation, we used 'particle' detection and edge detection methods to isolate and analyze the irregular structural features of the STM images taken during the decomposition and desorption reactions.

For those images taken at initial stages of oxide removal (figure 6), an analysis of the voids provides not only a measure of the sum total void area on the surface, but also a measure of the void density as a function of area. Figure 13 is an example of the image analysis for voids. Here, for the same image as shown in figure 6(c), void areas are selected by sequential application of a spatial median filter to remove local noise in the image, a background subtraction to remove the step edge and terrace slope, and a thresholding function to highlight the voids. These voids are then analyzed for area and shape. The sum of the void areas is a measure of the fraction of the oxide layer which has been desorbed, and the number of voids corrected to the image area is the surface void density. By counting a histogram of void areas and again normalizing to the image area, a density distribution is measured. This surface void density as a function of void area is plotted in figure 14 for the three images shown in figure 6. From this plot it is apparent that the increased total void area at 13% desorption results from the voids of larger area but lower density. These density versus area plots can be used to understand the growth dynamics of voids as desorption and decomposition proceeds, and will be discussed in more detail in the following section.

On imaged surfaces consisting mostly of the clean Si(100)-(2×1) structure, it is possible to quantify the terrace edges in the image. In figure 15 the edges have been highlighted. In this case the image processing analysis required application of a local average to smooth structures on the terraces, followed by a local derivative function to accentuate the edges

between terraces. Next a threshold function is applied to select the edges, and the resulting lines are uniformly thinned to a single pixel width. At this point the image is analyzed for total length of edges, and the value normalized to the image size. For this illustration the edge outlines were overlaid onto the original image producing figure 15. This analysis has been performed where edges are present on the clean Si(100) images, on the images of late stage desorption, and complete removal of oxides. The results are tabulated in the edge density column in table 1.

Image Interpretation

From the structural information contained in STM images at different stages of the removal of oxide layers from silicon, it is possible to examine the spatial mechanism of the decomposition and desorption reaction. Considered here are two proposed spatial mechanisms for this reaction and the consequences of these mechanisms as compared to the results presented here. In these proposed mechanisms the silicon source for the desorbing SiO species differs. For the first mechanism, the source is the silicon to which the oxygen is locally bound; and for the second mechanism, the source is silicon which diffuses from neighboring clean surface to the oxide boundary.

The two mechanisms proposed here are similar in that both require desorption to occur at boundaries between oxide and clean silicon. In other words, desorption occurs from the perimeter of voids in the initial stages of oxide removal, and from the perimeter of oxide islands in later stages after the voids have begun to grow together. Both mechanisms also require an initial nucleation of voids at the surface.

One difference between the two mechanisms is the energetics of bond breaking to form the desorbing SiO species. In the first model both Si-O bonding and Si-Si bonding to the substrate would be involved in desorption, whereas for the second mechanism a silicon atom diffuses to the oxide boundary and only Si-O bond cleavage is required.

In the perimeter silicon source mechanism, desorption is purely a local phenomenon at the oxide edge, and the growth rate of voids has structural dependence only on the perimeter. Assuming a rate limiting step for the reaction mechanism dependent only on the void perimeter, the quasi-first order growth rate equation for an individual void is given by:

$$\frac{\partial A}{\partial t} = g_p P. \quad (1)$$

Here A is the void area, t is time, P is the void perimeter, and g_p is a constant for the void area growth rate which contains the temperature and local

coverage dependence. Making the assumption that $P \propto \sqrt{A}$ (though not necessarily in the ratio of a perfect circle) the rate law becomes:

$$\frac{\partial A}{\partial t} = c g_p \sqrt{A} . \quad (2)$$

Integration yields an area growth law for this model of:

$$A(t) = (k_p t + \sqrt{A_0})^2 . \quad (3)$$

Here the constant k_p is the temporal growth rate for void area at a given local coverage and constant temperature, and A_0 is the initial void area. From this relation it is clear that initial void size determines the size as desorption proceeds, and from equation (2) the area growth rate has only weak dependence on void area. This model corresponds to a similar desorption model where islands all desorb from a surface with identical rate of decrease in diameter.¹⁸

If, on the other hand, the desorption reaction requires a source of silicon other than that already present at void perimeters, the reaction must be described by a more complex rate law. For the second mechanism it is assumed that the source of diffusing silicon to the perimeter of a given void is the area contained within that void. Published STM results¹⁹ and theoretical calculations²⁰ report silicon atom on Si(100) diffusion constants which indicate that at the temperatures employed for oxide desorption the surface diffusion area of silicon atoms is much greater than the measured void areas. The amount of diffusing silicon atoms available at the perimeter, to a first approximation, is then proportional to the void area, and therefore the growth rate must also be proportional to the void area. For this second mechanism, the growth rate for a single void is quasi-second order, depending proportionally on both perimeter and area of the void:

$$\frac{\partial A}{\partial t} = g_{pa} P A . \quad (4)$$

Here the rate constant is g_{pa} . Substituting for the perimeter as before:

$$\frac{\partial A}{\partial t} = c g_{pa} A^{\frac{3}{2}} . \quad (5)$$

This integrates to the following law:

$$A(t) = \frac{1}{\left(\frac{1}{\sqrt{A_0}} - k_{pat}\right)^2} \quad (6)$$

Here the growth constant, k_{pa} , for all voids must be positive. In this formulation, the area of voids with large initial areas grows more rapidly than those with small initial areas. From the differential rate law in equation (5), it can be seen that the growth accelerates as the void area increases, with a stronger area dependence than for the first order reaction mechanism.

From the measured constant void density for initial desorption, it can be assumed that voids must nucleate at the very start of desorption and that no new voids are nucleated as desorption proceeds. Given that as desorption initiates voids nucleate on the surface with an initial distribution of areas, that no new voids are nucleated during the reaction, the evolution of the area distributions which would arise from both mechanisms is determined by that initial distribution. A comparison of the calculated evolution of density distributions from equations (3) and (6) with that actually measured at early stages of void growth can show which of the two mechanisms is consistent with the desorption reaction. The comparison must, however, be made as a function of total void area, not time, as total desorption is the measurable quantity for reaction progress in STM images.

Neither of the two proposed mechanisms predicts the density or size distribution for initial void formation. Void densities measured for the images shown in figure 6 remain constant at $\approx 1 \times 10^{-4}$ per \AA^2 . Over the approximately 9 fold increase in total void area from desorption, this is interpreted to mean that there is no further nucleation of voids after the onset of desorption. STM images exhibit no indication of the nucleation sites for voids. The void density measured for these coverages is a factor of three less than the vacancy density measured for clean surfaces, and therefore it is possible that a subset of the initial surface vacancies are the localized nuclei for desorption voids. Images taken after room temperature oxidation show a surface without local order, and LEED patterns no longer show the (2×1) periodicity. There is no indication that initial clean atomic scale structure of the surface is even preserved after oxidation. Without further investigations no explicit determination the nature of the nucleation of oxide voids can be made.

For the purpose of calculating the the void distribution evolutions as modeled in equations (3) and (6), the distribution measured at low desorption levels (1.5% from figure 14), will constitute the initial distribution. This area distribution is projected in time by applying the derived growth laws to a given void area and maintaining the number density of that collection of voids constant as the area grows with time. To apply this method, and to compare

calculated distributions, a functional means of describing the distributions with an inverse exponential law was developed.

The density versus area distributions shown in figure 14 are best described by a two parameter fit to the following area distribution law:

$$\rho_{\text{void}}(A) = \frac{\xi}{A^{\sigma}}, \quad (7)$$

where $\rho_{\text{void}}(A)$ is the number density of voids with a given area, A , per unit area on the surface. The exponent, σ , essentially describes the shape of the distribution curve, and multiplication factors, ξ , the extension away from the axes. The two parameters are extracted from these data by taking a log-log plot of the area versus density and fitting the resulting line using a linear least squares analysis. The slope yields the negative of the exponent σ , and the intercept the log of the multiplication factor ξ . The resulting fits are plotted with the data in figure 14. From examination of figure 14 it can be seen that void growth is dominated by the increased density of larger void areas. This is reflected by a decrease in the exponent σ , while the multiplication factor remains relatively constant.

Application of the two modeled growth equations to the initial distribution, as measured for the lowest desorption level, produces calculated results for time evolution as shown in figure 16. For each graph a representation of the mechanism is included. An appropriate time interval and growth constant are chosen for each of the two growth models derived in equations (3) and (6) such that the total void area increases by a factor of 10, similar to the range of increase measured for figure 6. At a given time the total void area for a calculated distribution is simply the sum of the products of the area and the density at that area:

$$\text{Total Simulated Void Area} = \sum_A \{A \cdot \rho_{\text{void}}(A)\}. \quad (8)$$

The void area evolution resulting from the two growth laws can best be compared to the measured data by visual inspection of the distributions shown in figure 14 and those calculated for figure 16. For a first quasi-order mechanism, in which growth depends only on the void perimeter (equation 3), the distribution curves in the top part of figure 16 maintain a nearly constant shape and evolve evenly toward the larger void areas. As a result, these curves when fit to equation (7) have simultaneously increasing exponents σ , and multiplication factors ξ . The same two parameter log-log fitting

procedure which was used for the data derived by image analysis was applied to these growth simulations. For the quasi-first order mechanism, the parameter evolution with increasing desorption, relative to the initial total void area, is shown by the broken lines plotted in figure 17.

In contrast the lower half of figure 16 shows that for a growth rate dependent on both area and perimeter, the total increase in void area appears as an increase in the area of larger, lower density voids. Smaller voids do not increase in size as rapidly as larger voids in this model. The fitting parameters for this law, shown in figure 17 as solid lines, show a relatively constant multiplication factor, and a decreasing exponent as total void area increases.

The modeling inverse exponential parameters and are plotted in figure 17 in comparison to the single point values derived from the data fit to density distributions shown in figure 14. The error bars in the figure are derived from the parameter fitting functions and represent a 95% confidence limit.

Qualitatively the measured density distribution evolution shown in figure 14 is more consistent with the calculated distribution for the quasi-second order mechanism shown in the bottom part of figure 16. The measured density distributions show preferential growth of large voids, as was predicted for a mechanism where the reaction rate limiting step involves diffusing silicon atoms reacting at void perimeters to desorb as SiO. A more quantitative comparison can be made from the fitting parameters as plotted in figure 17. The inverse exponential parameter evolution for both models are plotted together using a broken line for the perimeter silicon source mechanism and a solid line for the diffusing silicon atom source mechanism. The top graph shows the relative change in the exponent factor, σ , and the bottom graph the relative change in $\log(\xi)$, the multiplication factor. The measured distributions, depicted at points with associated error bars, are more consistent with the evolution shown by the solid curves, which are derived from the calculated distributions for the quasi-second order mechanism. By both appearance and quantitative analysis, the measured evolution of void area density distributions is consistent with a desorption mechanism where diffusing silicon atoms from within voids constitute a limiting reagent for the reaction.

The modeling of the two growth mechanisms proposed here, and the calculations made for each, are necessarily simplistic. Neither accounts for the initial formation of voids, and neither allows for the coalescence of voids at higher total desorption. At the desorption stage imaged in figure 6(c) the larger voids have already begun to grow together and smaller voids have been consumed by larger voids. If roughly 13% of the total surface area is covered by large voids, then 13% of the initially smaller voids have coalesced into the larger voids and will no longer be counted, producing a lower measured

density; this effect is apparent for smaller void area in the lower curve in figure 14. The evolving shape of voids has also been neglected in the derivation of the area growth functions. From the highlighted void areas in figure 13, it can be easily seen that by this point in the desorption reaction the void perimeters have become convoluted with respect to the initially small round voids imaged at lower total desorption. In fact, for the images in figure 6, the measured ratio of void perimeters to square root areas increases with increasing desorption: from $3.97 (\pm 0.04)$ at 2% desorption to $6 (\pm 0.1)$ at 13 % desorption (for a circular void the ratio has a minimum value of 3.54). The simple linear growth rate dependence on void area derived for the quasi-second order mechanism also assumes that void area is the only factor which determines in the quantity of diffusing silicon atoms available to react at the perimeter. The step edge roughening within voids should, in general, increase the availability of diffusing silicon atoms to react at the void perimeter. The consequence of both these effects is that the value of the growth rate, k_{pa} in equation (6), is not constant as growth proceeds, but rather decreases, thereby effectively increasing further the growth rate for larger voids.

Additionally, analysis of the STM image data has not accounted for the resolution limit in the quantification of small area voids, other than to exclude the smallest sized void densities from the log-log parameter fitting. In general this should not affect the results presented here.

The images of the surface at later stages of desorption do not provide quantitative information regarding the removal mechanism for oxide layers; however a qualitative accounting for the roughening of the surface must be consistent with the desorption mechanism. Consider that desorption of a monolayer oxide removes only the equivalent of the top layer of silicon. During desorption it is known that the oxide does not diffuse,¹⁰ and that silicon diffusion is facile.¹⁹ If the mechanism of silicon desorption from the perimeter were correct, it is possible that silicon atom diffusion concurrent with the oxide desorption could cause surface roughening, but it is unlikely to cause pitting of the surface. Observations of surfaces with local carbon contamination which pins local islands on the Si(100)-(2×1) surface show no evidence of pitting after heating to temperatures equal to the desorption temperature used here. Nor is there any evidence of roughening if a clean sample is heated to similar temperatures.

In contrast a reaction model which removes silicon from within voids would leave a ledge adjoining remaining oxide at the same terrace level as the remaining oxide. The larger voids in figure 6(c) show just such a formation of perimeter ledges. The images of the surface after further desorption, such as figures 9 and 10, also show oxide islands on the top silicon layer, usually surrounded by silicon on that same layer. This would be expected if silicon is not removed from the oxide boundary. For the diffusing silicon source mechanism, the partial removal of an initial single monolayer oxygen coverage

is expected to produce a surface with more pronounced pitting than for lower initial coverages, where the initially open network of oxide would allow for silicon atom diffusion between existing oxide patches. This is exactly what is observed in figures 9 and 10.

The issue of the apparent removal of more than 1ML of silicon in the images of figure 8 can not be resolved by either desorption mechanism discussed here. Three possible explanations exist. First that the coverage calibration for oxide is incorrect. The saturation of adsorbed oxygen as measured by AES compares well with previous studies of molecular oxidation at room temperature where near monolayer oxygen coverages have been well characterized by other means. The saturation AES O_{KLL} intensity for O_2 exposure is twice that for H_2O exposure with a known $\frac{1}{2}$ ML saturation. From these arguments the saturation coverage is no more than 15% in error.

A second possibility is that the silicon is removed in some form other than SiO . The sublimation rate of silicon atoms from a clean silicon surface is negligible at the oxide desorption temperatures. Likewise silicon desorption catalyzed by desorption from on top an oxide island contradicts microscopic reversibility; if silicon atoms were to desorb from oxide then the reverse process would be unfavorable, but this contradicts the fact that the sticking coefficient of silicon atoms on silicon oxide is appreciable. This leaves open only the possibility that a Si_nO species is desorbing and is detected only as SiO by mass spectrometry. Testing this possibility is beyond the scope of a STM experiment.

A final possibility exists, and that is that the silicon remains on the surface. Either the surface structure rearranges and somehow floats the oxide islands to higher terrace levels, or the silicon diffuses to very low density defects on the surface and is not imaged by the STM.

None of the above explanations is particularly satisfying, and at this point the issue must remain unresolved.

Once the oxide is completely removed there is little evidence in the STM images to evaluate the reaction mechanism. The transformation from the pitted surface at nearly complete desorption of initial full monolayer coverages, to complete desorption with only roughened terrace edges, indicates that silicon diffusion at these temperatures is sufficient to anneal out island and pits. However there appears to be a kinetic barrier to complete smoothing of the terrace edges, and an even greater kinetic barrier to remove the $(2 \times n)$ reconstruction ubiquitous on the surface.

The $(2 \times n)$ structure has been frequently observed by LEED,¹⁴ and STM.¹⁵ Several analyses of the structure and its energetic stability have been previously published.²¹ Published images of homoepitaxy on $Si(100)$ often

show vacancy distributions in deposited islands of similar appearance to those imaged after oxide removal. The regular spacing of vacancy chains indicate long range forces must stabilize this surface configuration. Kinetic simulations show that vacancies in a top layer of silicon are not filled by homoepitaxy until covered by the next layer.²² The exact origin of the structure is unresolved, but its removal by high temperature heating is likely via removal of the top layer of silicon by sublimation.

As an aside we present here our interpretation the $c(4\times 4)$ structure. The observed domain structure and its apparent origin indicate the reconstruction is formed by the filling of pits or terrace edges remaining on the partially desorbed surface structure. A similar structure has been observed with STM for low temperature epitaxy on the Si(100) surface by Mo and coworkers.²³ They report a 'diluted-dimer' structure with a $2\times$ spacing in the dimer row direction. However, they observe only isolated rows, not two dimensional domains as here for the desorption of oxygen. In addition, a LEED study of surface disordering of Si(100) after the desorption of hydrogen has shown a $c(4\times 4)$ reconstruction.²⁴ A $c(4\times 4)$ pattern is regularly observed by LEED after the low temperature desorption of $\frac{1}{2}$ ML of adsorbed water.

Because this structure has been observed via STM on only a limited number of occasions, it is interpreted as a metastable reconstruction of slightly higher free energy with a small kinetic barrier before the formation of the $(2\times n)$ structure. On a sample with $< 1\%$ remaining initial oxygen, the initial formation of $c(4\times 4)$ domains was observed. These domains appeared only in the bottom of existing pits, or at the edge of terraces surrounding a pit. Complete removal of the oxide from this sample led to an increase in the reconstruction area, with 15% total surface area as $c(4\times 4)$ domains. Annealing to a temperature 75° higher removes the $c(4\times 4)$ domains.

The proposed atomic structure shown in figure 18 is the result of an extension to the interpretation that the $c(4\times 4)$ structure is formed by filling of pits on the surface. (A previously reported possible structure for the Si(100)- $c(4\times 4)$ surface by Pandey²⁵ is similar, however his structure shows dimers forming between rows, which are not observed in the STM images.) The intermediate height maxima observed by STM in this model are top layer dimers which have filled in between existing dimer rows on the lower layer. This site is the same as predicted by potential energy barrier calculations for the formation of new dimer rows by homoepitaxy.²⁶ These new on-top dimers break only alternate dimer bonds on the lower layer, thus these top layer dimers — and their associated maxima in the STM image — are shifted down and toward the unbroken lower level dimers. The remaining holes where the underlying dimers have been broken can either remain empty, appearing as a

pit to the STM, or can be filled with an on top dimer at the expected height for a completely formed dimer. Adjacent rows alternate the location of the underlying remaining dimerization. This explains the '4×' periodicity along a row corresponding to two underlying rows, and the orthogonal inter-row '4×' periodic structure of the c(4×4) domains. Of course, as STM is not a purely structural measure of the surface, this interpretation may be flawed; still, the surface structure is not expected to significantly deviate from the constant current profiles measured for filled states on the surface. A more complete analysis would require calculation of constant charge density contours for this proposed structure.

Both the (2×n) and c(4×4) structures have decreased surface atom density as compared to the clean and annealed Si(100)-(2×1) structure. The growth of silicon oxide at the surface certainly lifts the (2×1) reconstruction, and the disordered surface imaged by STM indicates that the original surface structure is likely even further disrupted. As desorption proceeds two things occur at once which effect the reforming of the (2×1) reconstruction. First silicon is removed from the surface as SiO desorbs. Second patches of clean silicon are opened as the spatially heterogeneous decomposition and desorption reaction proceeds. The clean surface is therefore reformed at the desorption temperature, where kinetic barriers likely exist between the observed (2×n) and c(4×4) structures and the complete (2×1) reconstruction. In fact, in every case where regions of clean silicon are observed after removal of an oxide layer, the dimer vacancy chains characteristic of the (2×n) reconstruction are imaged.

The vacancy chains also provide an additional source for diffusing silicon atoms. Thus when desorption proceeds as predicted by the silicon diffusion mechanism, the vacancy chains grow in length and density, or in the extreme case open a terrace to the next lower level by formation a pit. The (2×n) formation is certainly a consequence of the desorption and likely a source for the silicon component of desorbing SiO.

E. Conclusions

When a chemical process at a surface shows spatial inhomogeneity, and the reaction is either slow enough to be imaged, or the reaction can be interrupted for imaging, STM provides an ideal means to measure the structural consequences of the surface chemistry. For the reaction of inhomogeneous decomposition and desorption of silicon oxide layers the reaction modified surface has been imaged as desorption proceeds for initial oxygen coverages of one monolayer and lower.

Compared in this chapter are quantitative image analysis results of void areas as a function of total desorption with two reaction mechanisms. The results indicate void growth evolution consistent with a growth rate which depends on both void perimeter and area. The mechanism we use to explain this rate law is one which requires that the silicon source for desorbing SiO is from diffusing silicon rather than silicon to which the oxygen is originally bound. For thicker oxide layers it is clear that removal of SiO from an initial SiO₂ layer would require an additional source of silicon which originates in the voids formed by desorption of these thicker layers. However, the removal of initial oxygen coverages of one monolayer and below has no such requirement for excess silicon. One explanation of the inhomogeneity observed in the desorption of these thin oxide layers is an inhomogeneity of the initial oxide either structurally or energetically. Another explanation lies in the mechanism for decomposition of the oxide layer. If desorption occurs when diffusing silicon reaches an oxide boundary then the reaction itself is spatially inhomogeneous in the source of one reactant. In this model desorption can not proceed other than inhomogeneously at a boundary between clean surface and oxide.

It should be noted that the desorption rate predicted by the diffusing silicon mechanism contradicts that measured for thicker oxide layers.⁷ Without further STM experimentation on thicker oxide systems it is difficult to speculate on the reason for this inconsistency. The nature of the oxide layer, and the density of voids are clearly very different in the two cases, and the thin layer oxides may present a limiting case for the reaction mechanism.

Desorption likely initiates at 'pin hole' voids in the initial oxide and proceeds as these voids grow. The voids grow with a rate law which prefers the growth of larger voids, a trend substantiated by the measured change in void density versus area. At levels of partial desorption nearing complete removal of the oxide, the surface exhibits pitting for surfaces from which an initially complete monolayer oxygen coverage was removed. This is consistent with a model which inhomogeneously removes silicon from the surface via atomic diffusion on clean silicon surface to the oxide boundary. Incomplete initial layers do not show this pitting because the open network on the surface and the lower silicon requirement do not necessitate the removal of silicon from within isolated void regions of clean silicon.

Silicon surfaces are observed to roughen after complete removal of oxide layers with formation of metastable surface reconstructions with decreased surface atom density. The well ordered low defect density initial surface can be reconstituted by high temperature heating of the sample.

While the conclusions of this study are limited to monolayer and lower oxide coverages on Si(100), the quantitative use of STM surface imaging in chemical reactions of this nature provides a new and important tool in the investigation of surface reaction mechanisms.

References

- ¹ R.J. Wilson and S. Chiang, *Phys. Rev. Lett.*, **59**, 2329 (1987); and R.M. Feenstra, *Phys. Rev. Lett.*, **63**, 1412 (1989).
- ² R.J. Hamers, U.K. Köhler, and J.E. Demuth, *J. Vac. Sci. Technol. A*, **8**, 195 (1990);
Y.-W. Mo, R. Kariotis, B.S. Swartzentruber, M.B. Webb, and M.G. Lagally, *J. Vac. Sci. Technol. A*, **8**, 201 (1990); and
A.J. Hoeven, D. Dijkkamp, E.J. van Loenen, J.M. Lenssinck, and J. Dieleman, *J. Vac. Sci. Technol. A*, **8**, 207 (1990).
- ³ D.D. Chambliss, S. Chiang, R.J. Wilson, in **Structure/Property Relationships for Metal/Metal Interfaces**, eds. A.D. Romig, D.E. Fowler and P. Bristowe, Materials Research Society (1991).
- ⁴ Ph. Avouris and R. Wolkow, *Phys. Rev. B*, **39**, 5091 (1989).
- ⁵ F.M. Leibsle, A. Samsavar, and T.-C. Chiang, *Phys. Rev. B*, **38**, 5780 (1988);
J.P. Pelz and R.H. Koch, *Phys. Rev. B*, **42**, 3761 (1990); and
Ph. Avouris, I.-W. Lyo, and F. Bozso, *J. Vac. Sci. Technol. B*, **9**, 424 (1991).
- ⁶ Ph. Avoris and C. Cahill, *Ultramicroscopy* (to be published).
- ⁷ M. Liehr, J.E. Lewis and G.W. Rubloff, *J. Vac. Sci. Technol. A*, **5**, 1559 (1987);
and
G.W. Rubloff, *J. Vac. Sci. Technol. A*, **8**, 1853 (1990).
- ⁸ Y. Kobayashi and K. Sugii, *J. Vac. Sci. Technol. B*, **9**, 748 (1991).
- ⁹ Y.-K. Sun, D.J. Bonser and T. Engel, *Phys. Rev. B*, **43**, 14309 (1991).
- ¹⁰ Y.-K. Sun, D.J. Bonser and T. Engel (to be published).

- 11 D. Schmeisser, *Surface Sci.*, **137**, 197 (1984); and
W. Ranke and Y.R. Xing, *Surface Sci.*, **157**, 339 (1985).
- 12 Y.-W. Mo, B.S. Swartzentruber, R. Kariotis, M.B. Webb, and M.G. Lagally,
Phys. Rev. Lett., **63**, 2393 (1989).
- 13 Y.-W. Mo, R. Kariotis, B.S. Swartzentruber, M.B. Webb, and M.G. Lagally, *J.*
Vac. Sci. Technol. A, **8**, 201 (1990).
- 14 J.A. Martin, D.E. Savage, W. Moritz, and M.G. Lagally, *Phys. Rev. Lett.*, **56**,
1936 (1986).
- 15 T. Sakurai, T. Hashizume, I. Kamiya, Y. Hasegawa, N. Sano, H.W. Pickering,
and A. Sakai, *Progress in Surface Sci.*, **33**, 3 (1990).
- 16 H. Niehus, U.K. Kohler, M. Copel and J.E. Demuth, *Journal of Microscopy*,
152, 735 (1988).
- 17 IMAGE for the MacintoshTM, Public Domain software by Wayne Rasband of
National Institute of Health, Research Services Branch.
- 18 A.J. Slavin and E.P.B. Young, *J. Vac. Sci. Technol. A*, **8**, 2463 (1990).
- 19 Y.-W. Mo, J. Kleiner, M.B. Webb, and M.G. Lagally, *Phys. Rev. Lett.*, **66**, 1998
(1991).
- 20 G. Brocks, P.J. Kelly, and R. Car, *Phys. Rev. Lett.*, **66**, 1729 (1991).
- 21 A. Tamura, *J. Vac. Sci. Technol. A*, **8**, 192 (1990); and
T. Aruga and Y. Murata, *Phys. Rev. B*, **34**, 5654 (1986).
- 22 H. Metiu, *private communication*.
- 23 Y.-W. Mo, R. Kariotis, B.S. Swartzentruber, M.B. Webb, and M.G. Lagally, *J.*
Vac. Sci. Technol. A, **8**, 201 (1990).

- 24 K. Kato, T. Ide, T. Mishimori and T. Ichinokawa, *Surface Sci.*, **207**, 177 (1988).
- 25 K.C. Pandey, *Proceedings of the 17th International Conference on Semiconductors* (ed. D.J. Chadi & W.A. Harrison) p55 (1984).
- 26 Z. Ahang, Y.-T. Lu, and H. Metiu, *Surface Science Lett.*, **255**, L543 (1991).

Table 1 — Summary of structural Roughness as measured for different stages of oxidation and desorption.

Surface condition	Edge Roughness (smooth type)	Edge Roughness (jagged type)	Edge Density (Å length per Å ² area)	Surface Atom density (compared to idealized surface)
Ideal Surface (all smooth edges with 0.08° Vicinal orientation from [100])	1	1	1.03×10^{-3}	100%
Annealed clean surface	1.0 (+0.4)	1.3 (± 0.2)	1.4×10^{-3}	> 96%
1ML initial coverage 88% desorbed	(no continuous edges)		3.0×10^{-2}	(83% for exposed Si)
1ML initial coverage Complete desorption unannealed	≈ 1.3	≈ 2.6	3.7×10^{-3}	83% [78% inside c(4×4) domains]
0.3ML initial coverage Complete desorption unannealed	(no continuous edges)		1.7×10^{-2}	

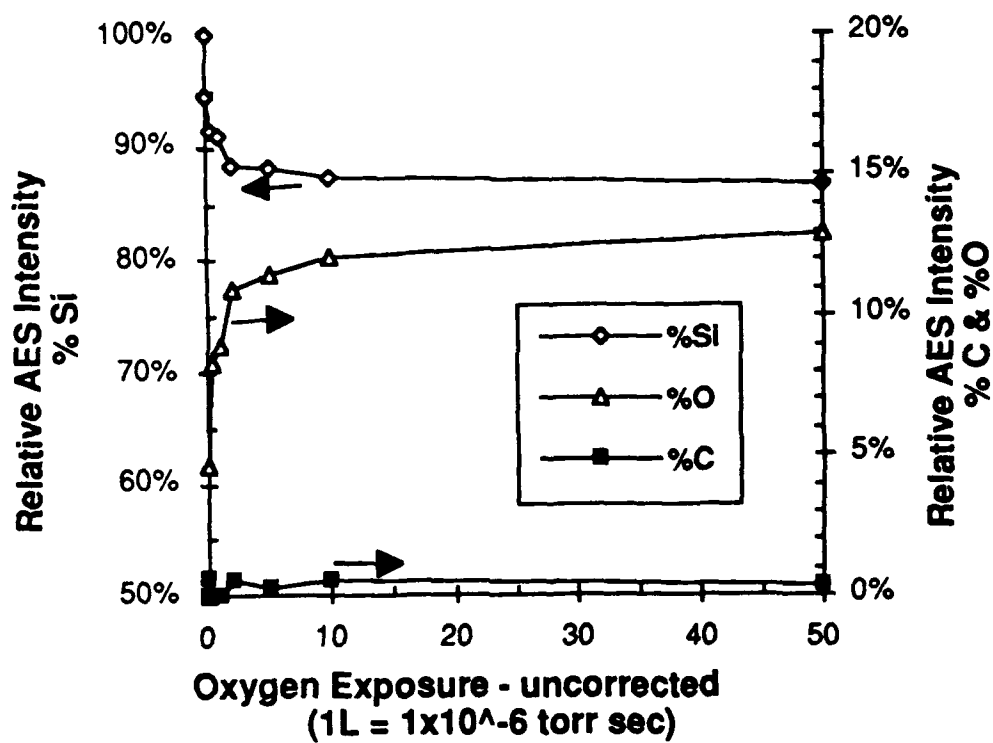


Figure 1 — Room temperature Si(100) oxidation uptake curve. AES corrected signal intensity as a function of oxygen exposure. Water saturation of the O_{KLL} peak was at $6.6 \pm 0.4\%$.

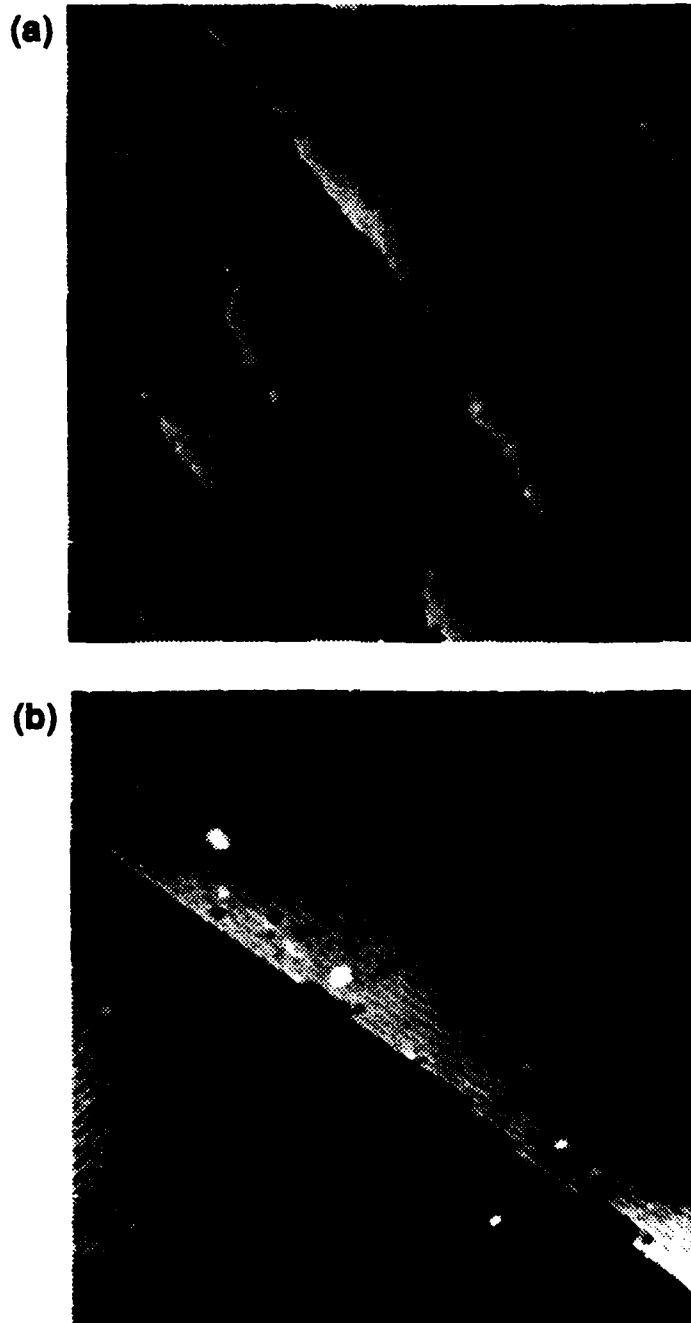


Figure 2 — Clean Si(100). Both STM images are taken at constant current with $i_{\text{tunnel}} = 1\text{nA}$ and $V_{\text{tip}} = +2\text{V}$. (a) Image dimension $\sim 4000\text{\AA} \times 4000\text{\AA}$. At this resolution only step edges and terraces are resolved. The alternating smooth and jagged step edges are clearly observed. (b) Higher resolution image $\sim 500\text{\AA} \times 500\text{\AA}$ showing (2×1) and (1×2) domains and a smooth type step edge.

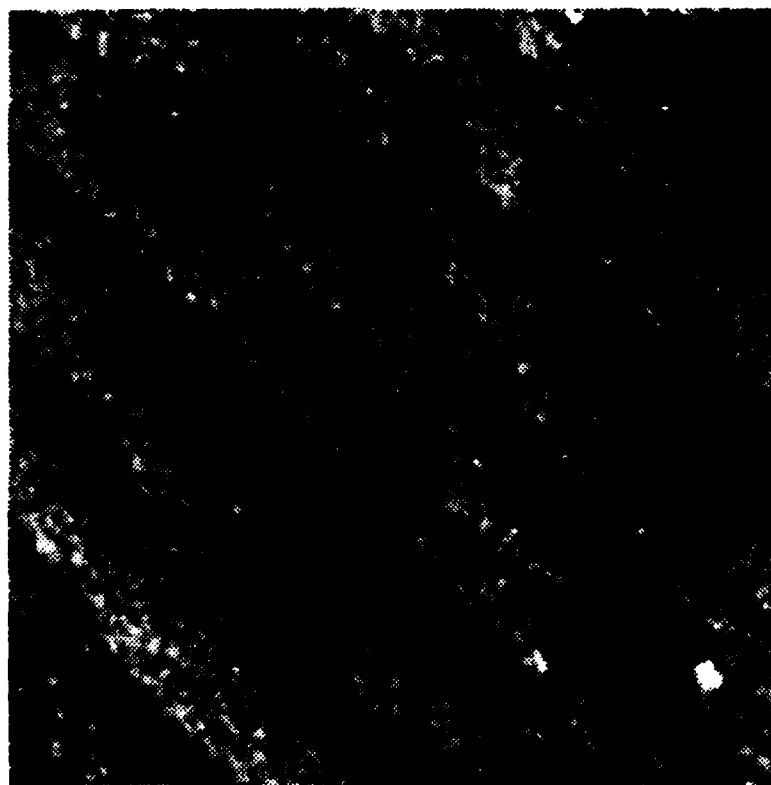


Figure 3 — Si(100) with 1 ML oxygen coverage. STM image taken at constant current with $i_{\text{tunnel}} = 1\text{nA}$ and $V_{\text{tip}} = +4\text{V}$. Image dimension same as fig. 5.2(a) $\sim 4000\text{\AA} \times 4000\text{\AA}$. Note that the terrace and step structure remains after oxidation.

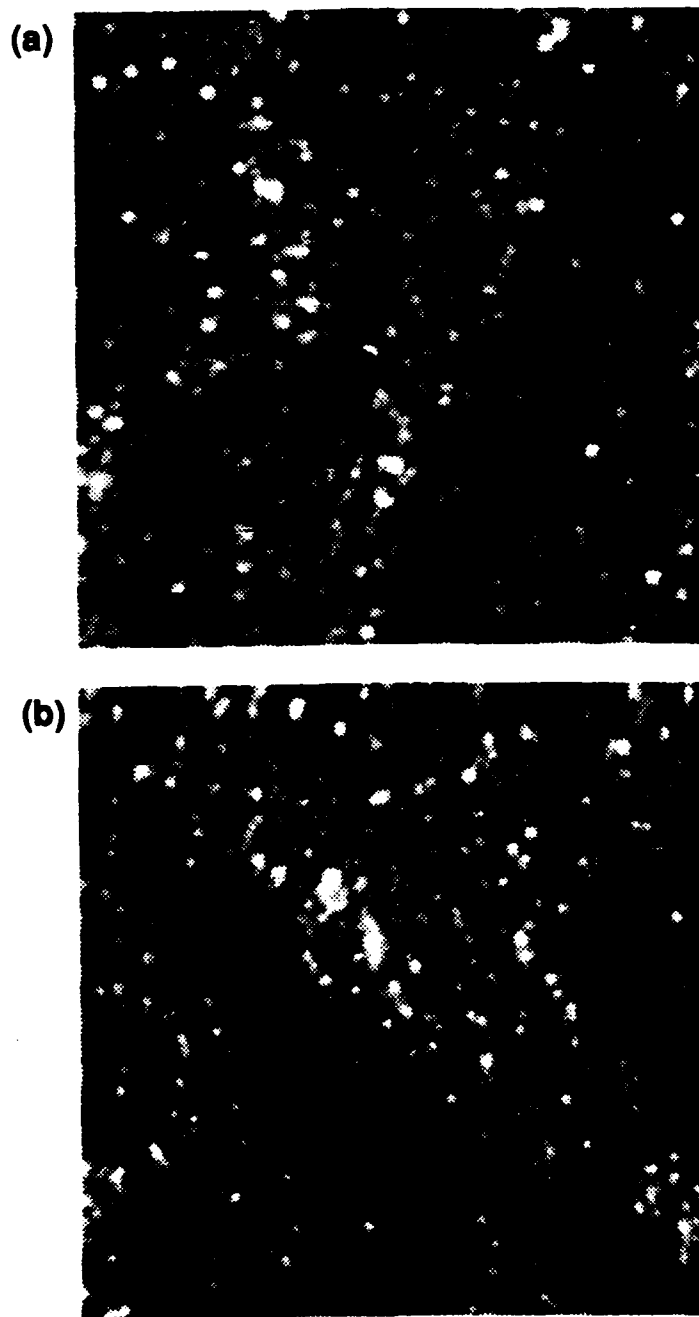


Figure 4 — Oxidized Si(100). Image dimensions are both $\sim 500\text{\AA} \times 500\text{\AA}$. (a) 1 ML coverage. (b) 0.3ML coverage.

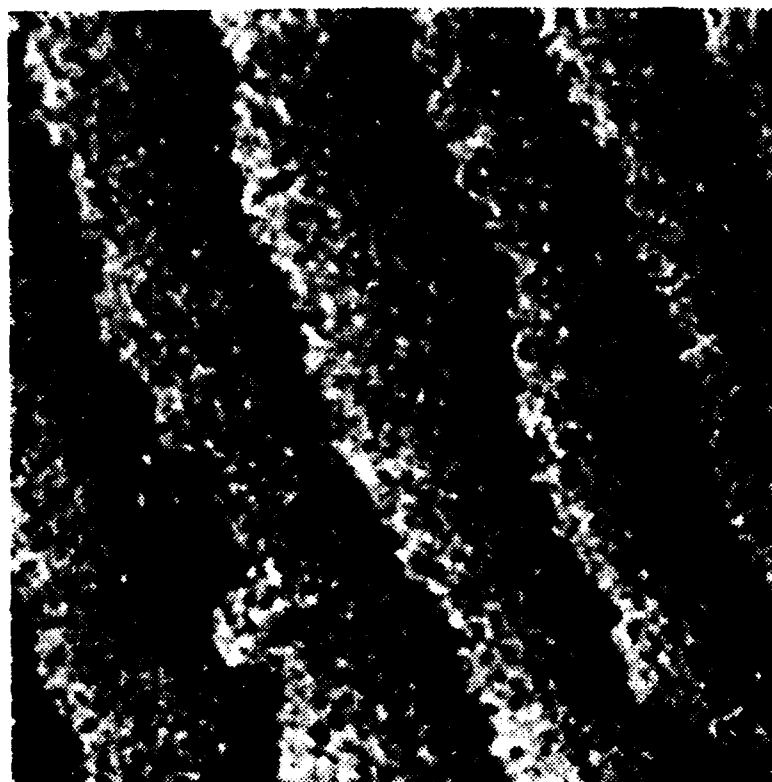


Figure 5 — Si(100) surface after initial desorption and void formation on a 1 ML initial oxide coverage after heating 15 seconds at 1000K. Measurement of total void area yields an estimate of 7.8% of the initial oxide desorbed. Image dimension is $\sim 4000\text{\AA} \times 4000\text{\AA}$.

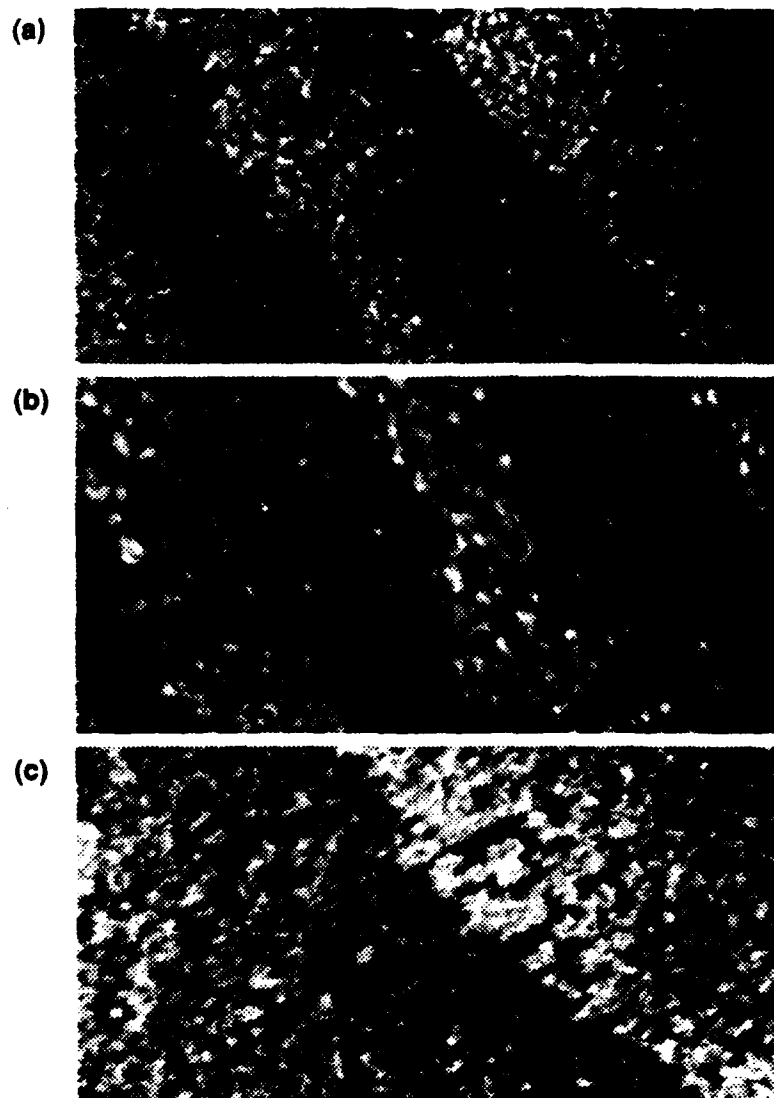


Figure 6 — Increasing total desorption from an initial coverage of 1 ML. All image dimensions are $\approx 2000\text{\AA} \times 1000\text{\AA}$. (a) 1.5% removed. (b) 8% removed. (c) 13% removed.

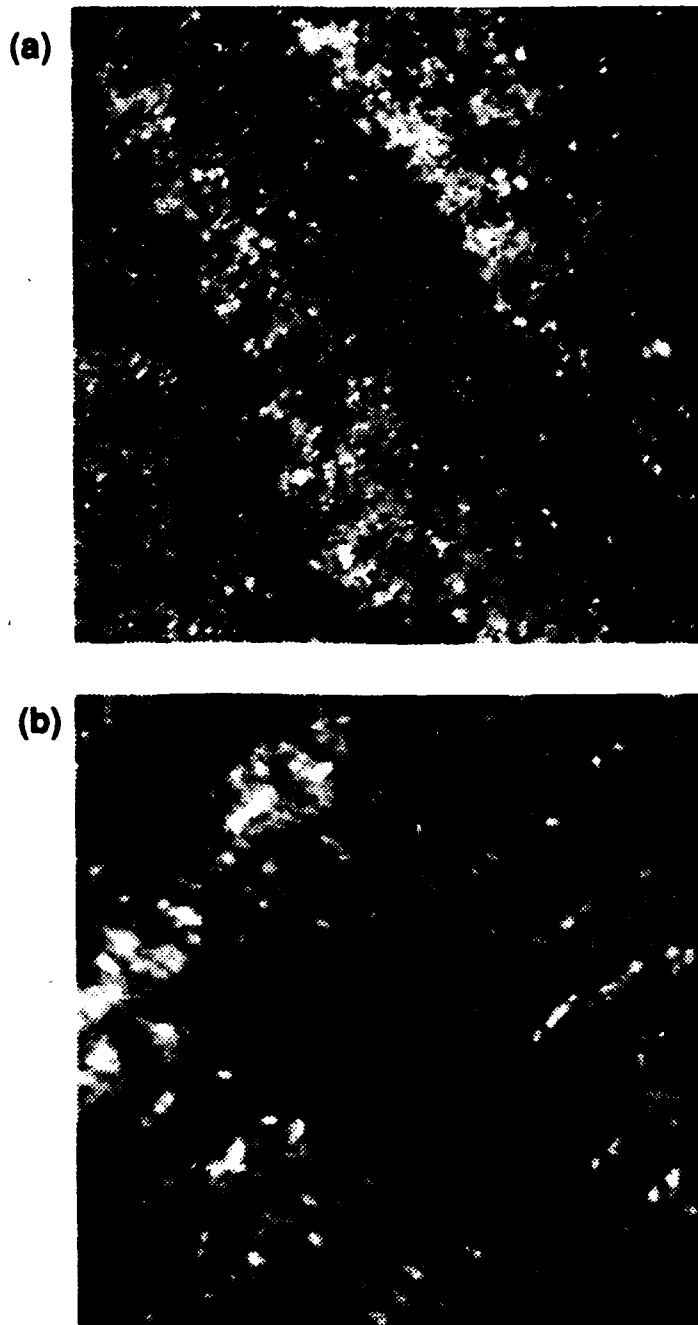


Figure 7 — Removal of >50% of an initial 0.3ML oxide layer.
Image dimensions are: (a) $\sim 2000\text{\AA} \times 2000\text{\AA}$, and (b) $\sim 500\text{\AA} \times 500\text{\AA}$.

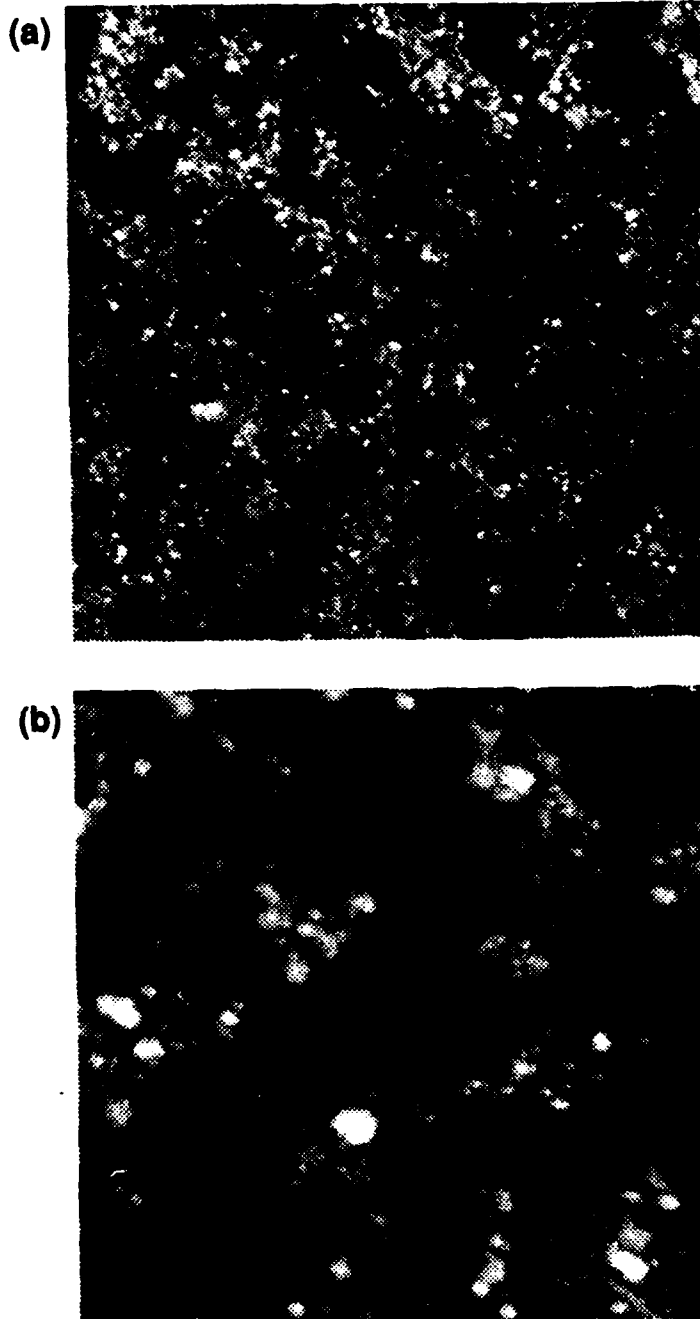


Figure 8 — Desorption of an initial 1 ML oxide layer to ~12% remaining oxide. (a) ~ 1750Å × 1750Å, and (b) ~ 450Å × 450Å.

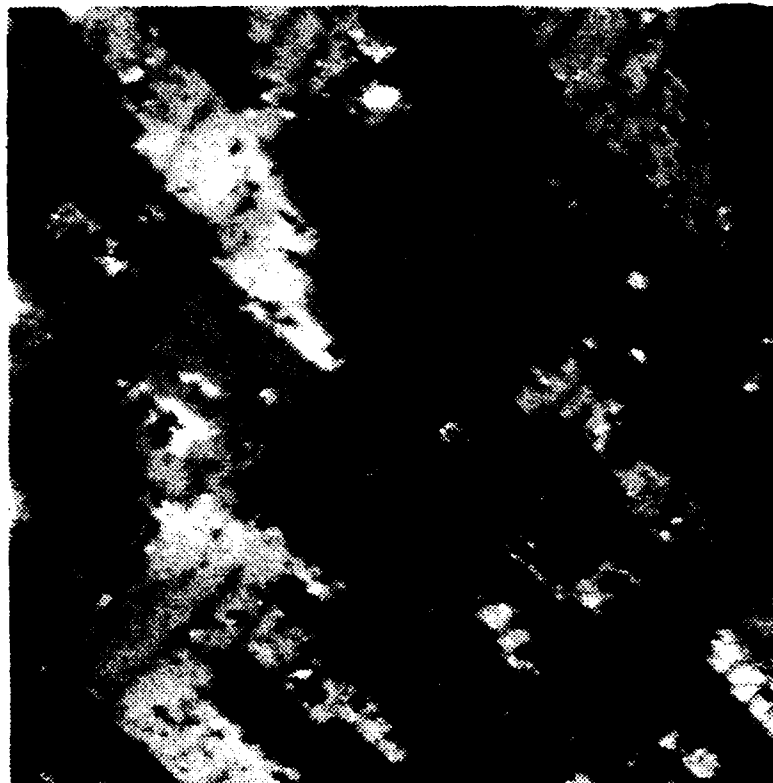


Figure 9 — Complete removal of an initial 0.3 ML oxygen coverage at 895K. Image dimension is $\sim 800\text{\AA} \times 800\text{\AA}$.

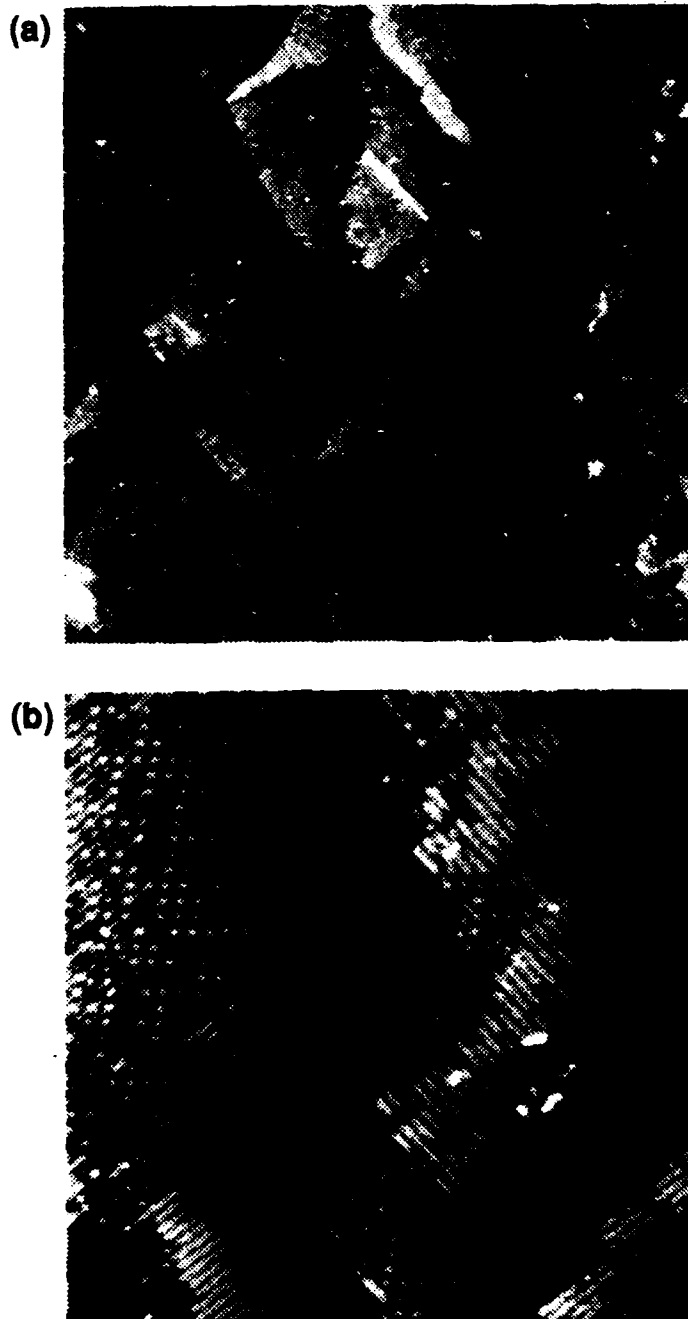


Figure 10 — Complete removal of an initial 1 ML oxygen coverage at 1000K. Image dimensions are: (a) $\sim 4000\text{\AA} \times 4000\text{\AA}$, and (b) $\sim 520\text{\AA} \times 520\text{\AA}$.

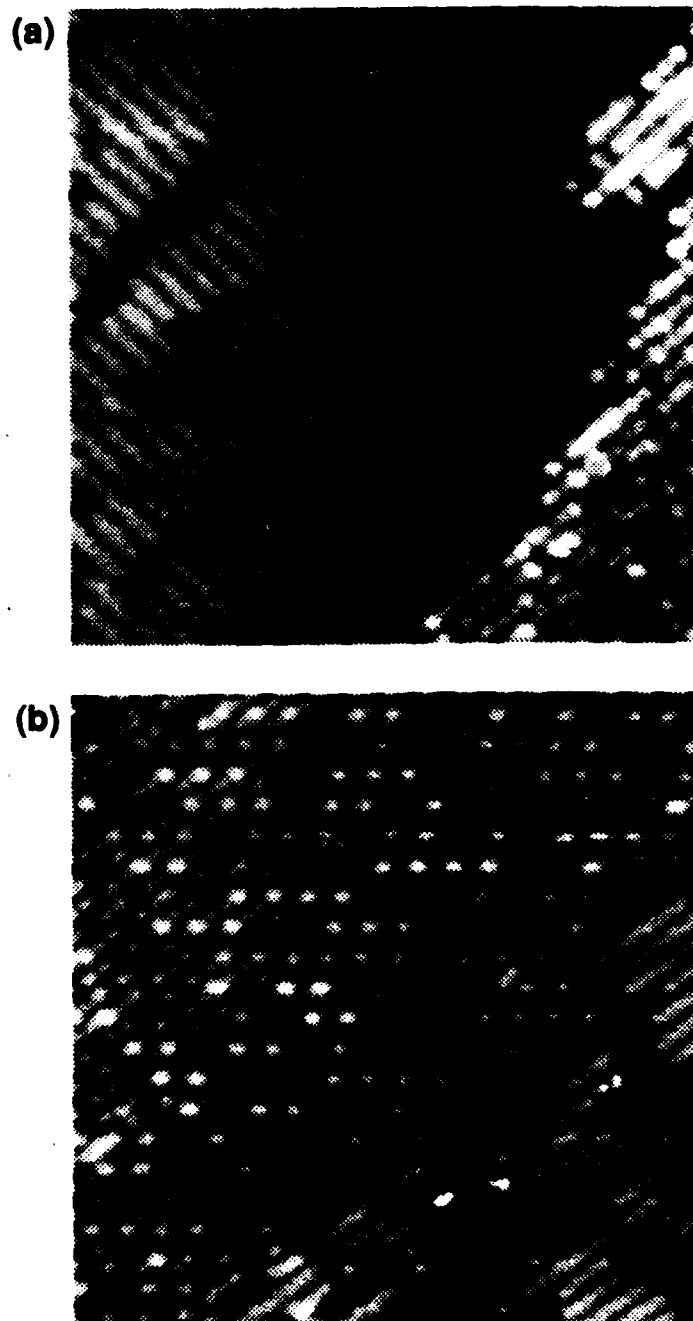


Figure 11 — Surface reconstruction details for complete removal of an initial 1 ML oxide at 1000K. Image dimensions are $\sim 200\text{\AA} \times 200\text{\AA}$. (a) Shows the (2×1) structure vacancy chains perpendicular to the dimer rows, and (b) shows the $c(4 \times 4)$ reconstruction both with lowered surface atom density.

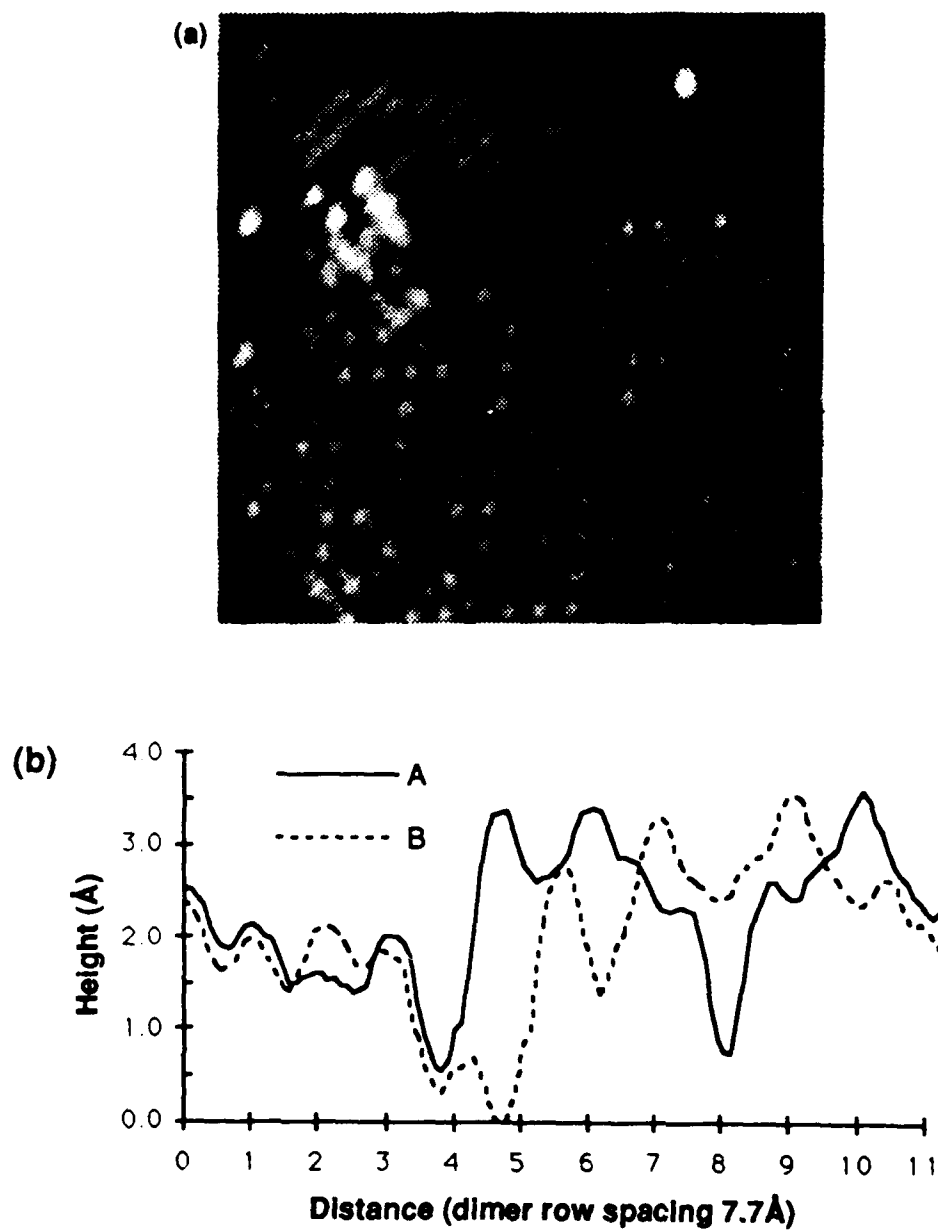


Figure 12 — STM image and line profiles of the Si(100) - $c(4 \times 4)$ reconstruction. (a) Image dimension is $\sim 200 \text{ \AA} \times 200 \text{ \AA}$. The $c(4 \times 4)$ unit cell is outlined in the lower center of the image. (b) Line profiles are taken between the arrows drawn on the image. The profiles show the periodicity within the reduced density dimer rows as well as the alignment with the underlying dimer rows. The alternating structure is shown by the shift in structural features between the two adjacent rows.

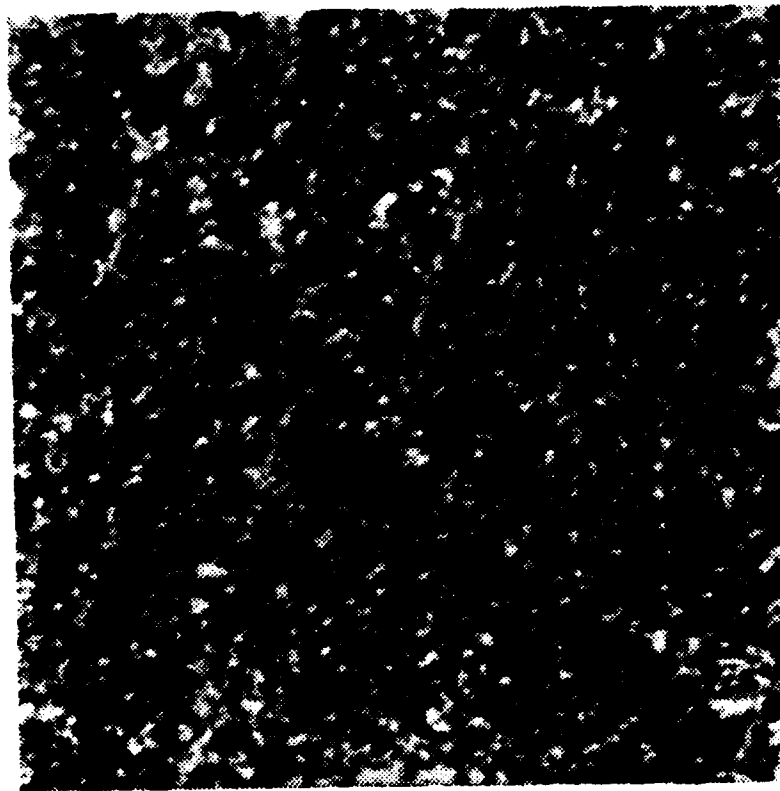


Figure 13 — Illustration of image processing used to quantify voids. This is the same image as shown in figure 5.6(c). The image processing is described in the text.

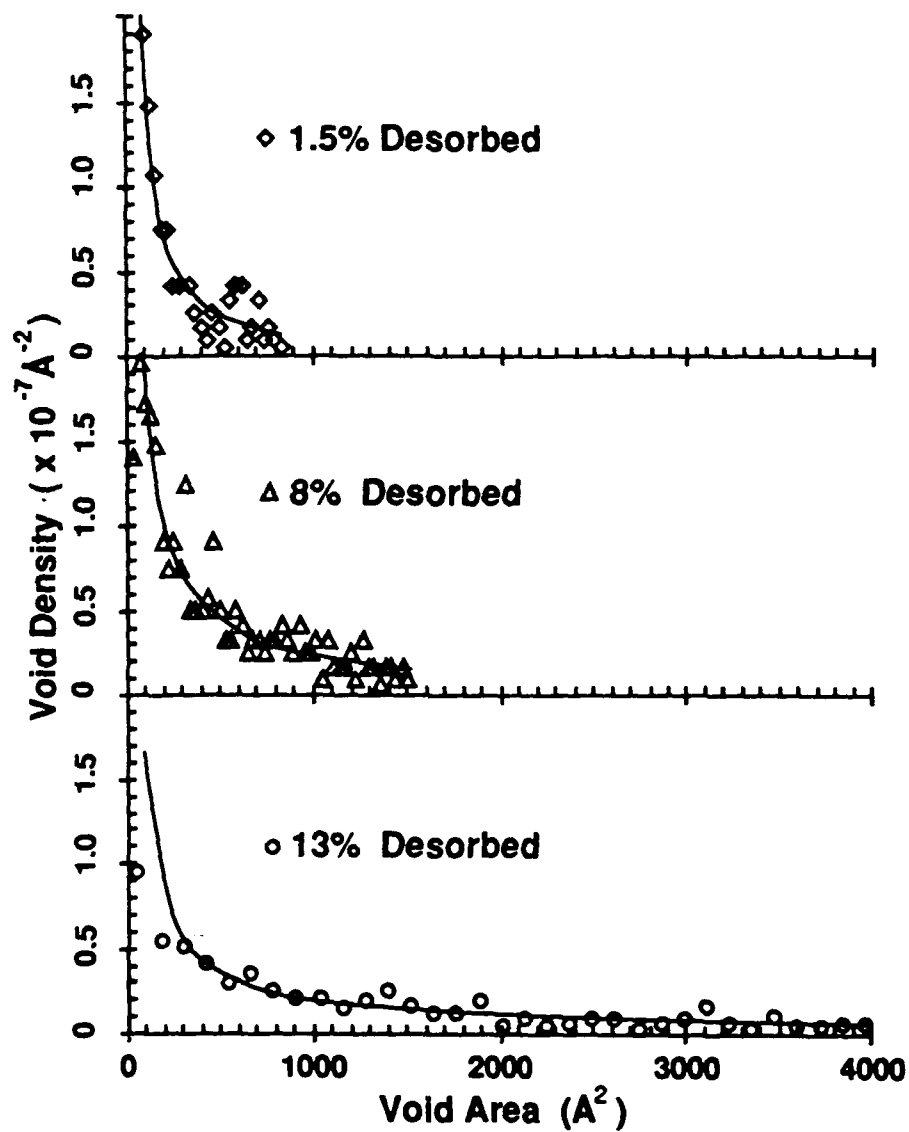


Figure 14 — Void density plotted as a function of void area for the images shown in figure 5.6. Lines are fit to an inverse exponential

distribution law, $\rho_{\text{void}}(A) = \frac{\xi}{A^\sigma}$.

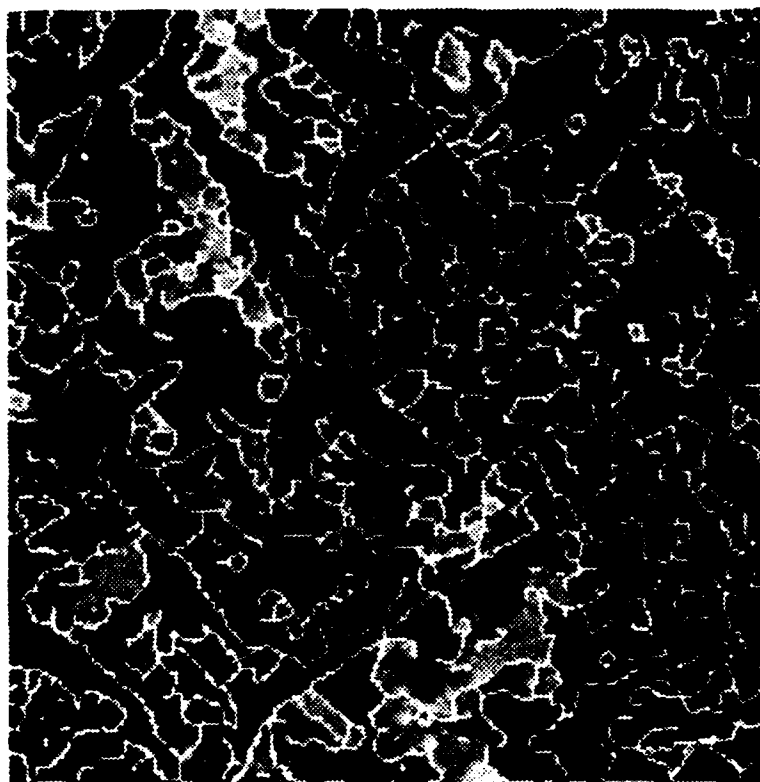


Figure 15 — Edge detection image processing. Surface has <1% remaining oxide from an initial 1 ML coverage. Image dimension is $\sim 2000\text{\AA} \times 2000\text{\AA}$. Edge highlighting procedure is described in the text.

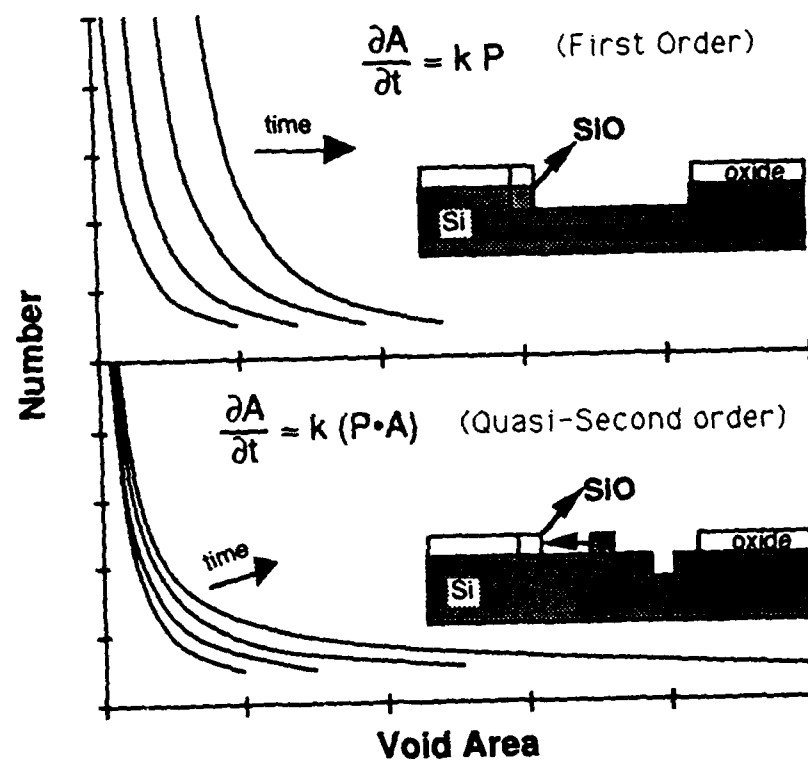


Figure 16 — Modeled void growth for increasing time. Top for void perimeter desorption mechanism, bottom for diffusion mechanism. Inset diagrams show representation of reaction mechanism.

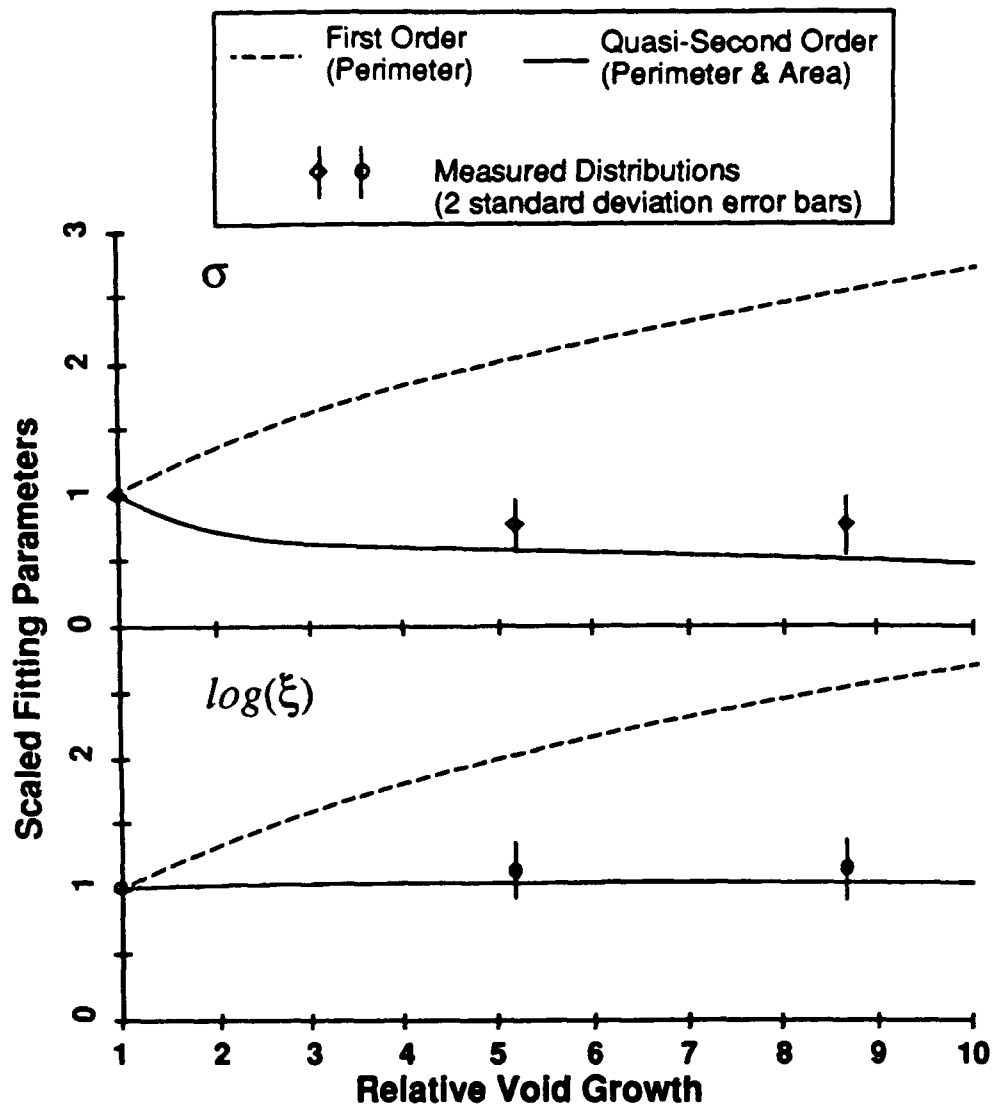


Figure 17 — Inverse exponential distribution fitting parameters for measured data from figure 5.14 and calculated for 5.16. Points (circle and diamond) are from measured void area density distribution with error bars derived from curve fitting statistics. The broken line is calculated for perimeter Si source mechanism, and solid line for diffusion Si source mechanism. All values plotted are normalized to that for the measured distribution with the lowest total void area.

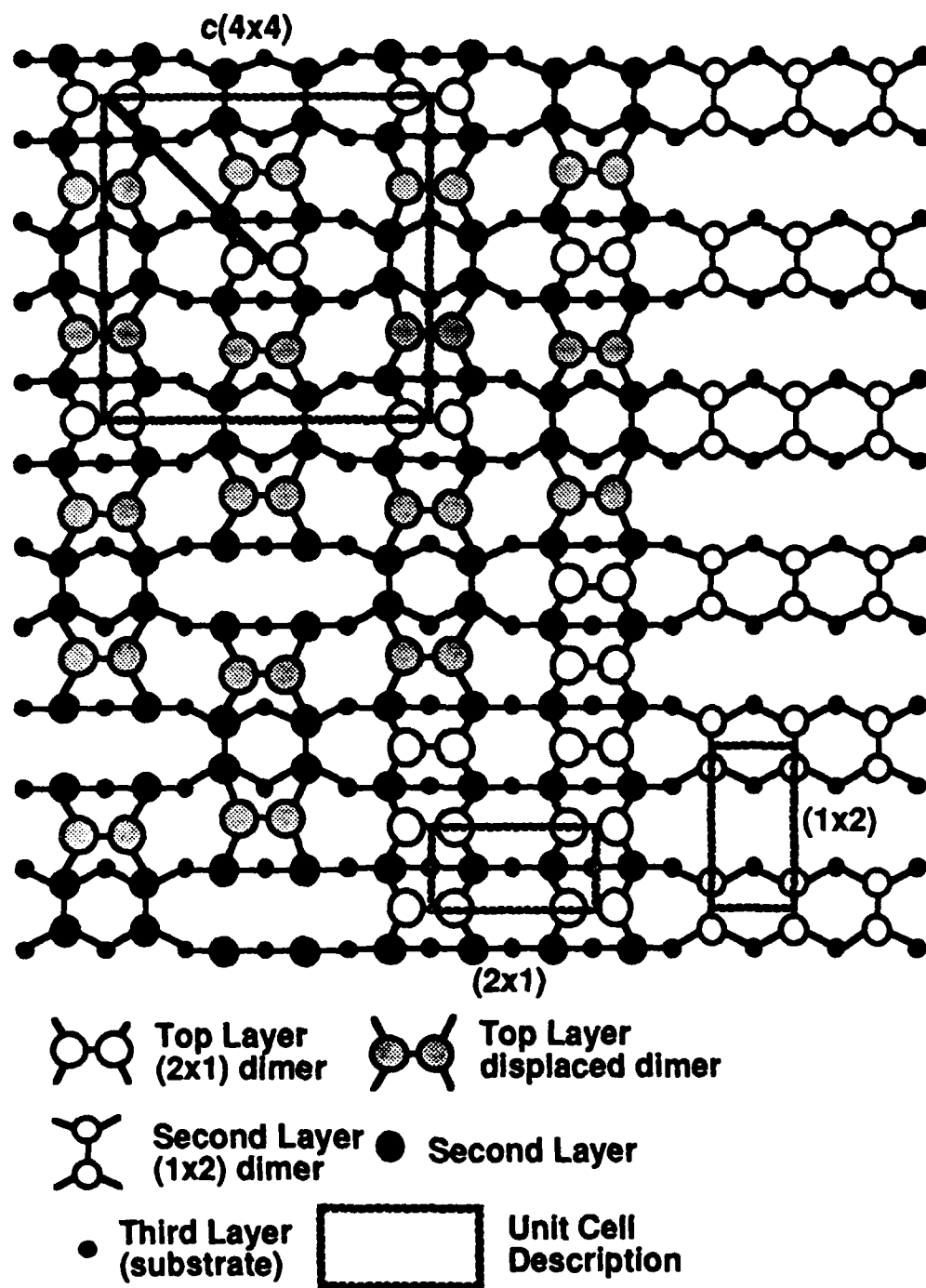


Figure 18 — Proposed structure for the $c(4 \times 4)$ reconstruction observed after complete removal of oxide layer, prior to annealing.

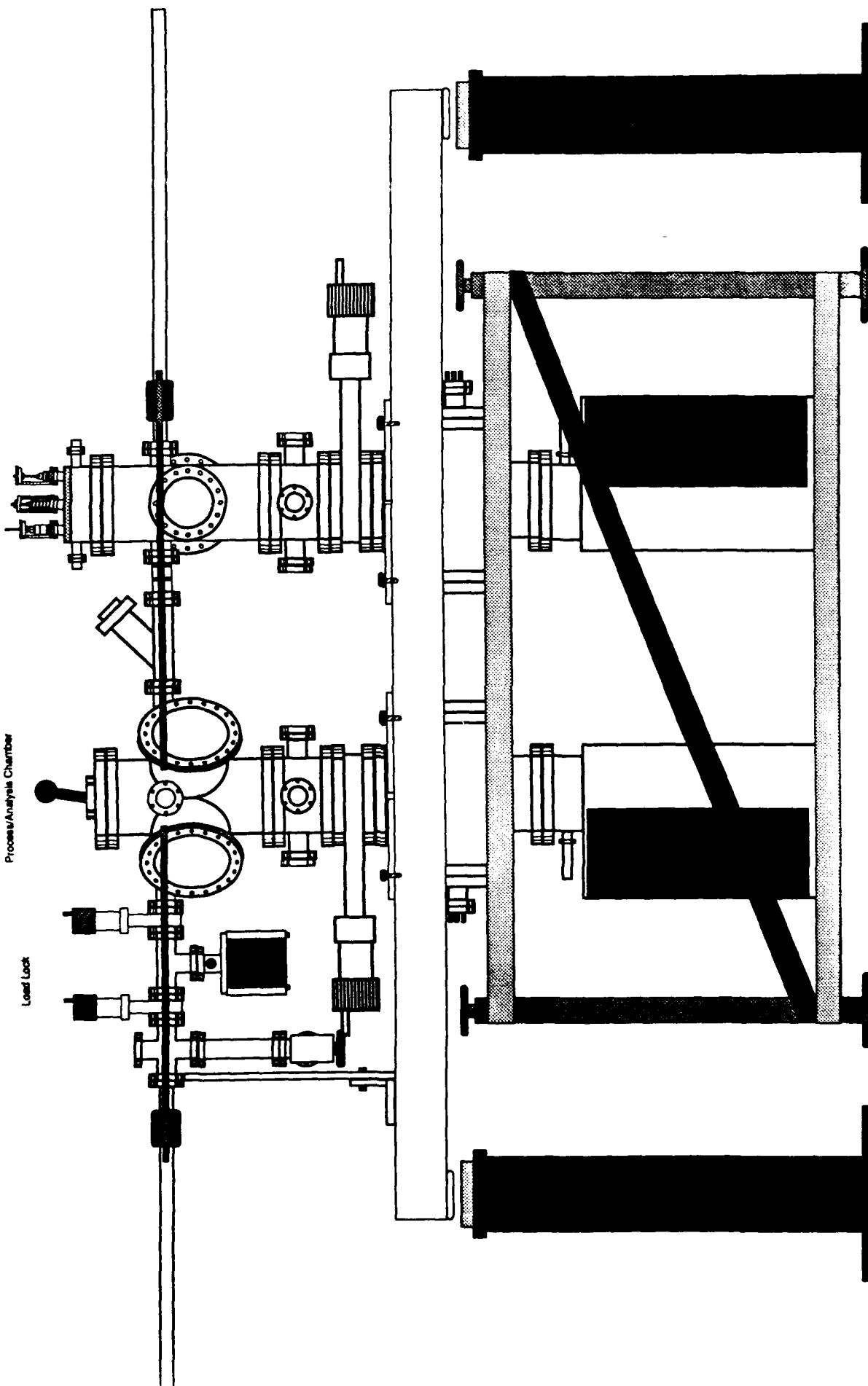
APPENDIX

New Microscope Chamber Side View

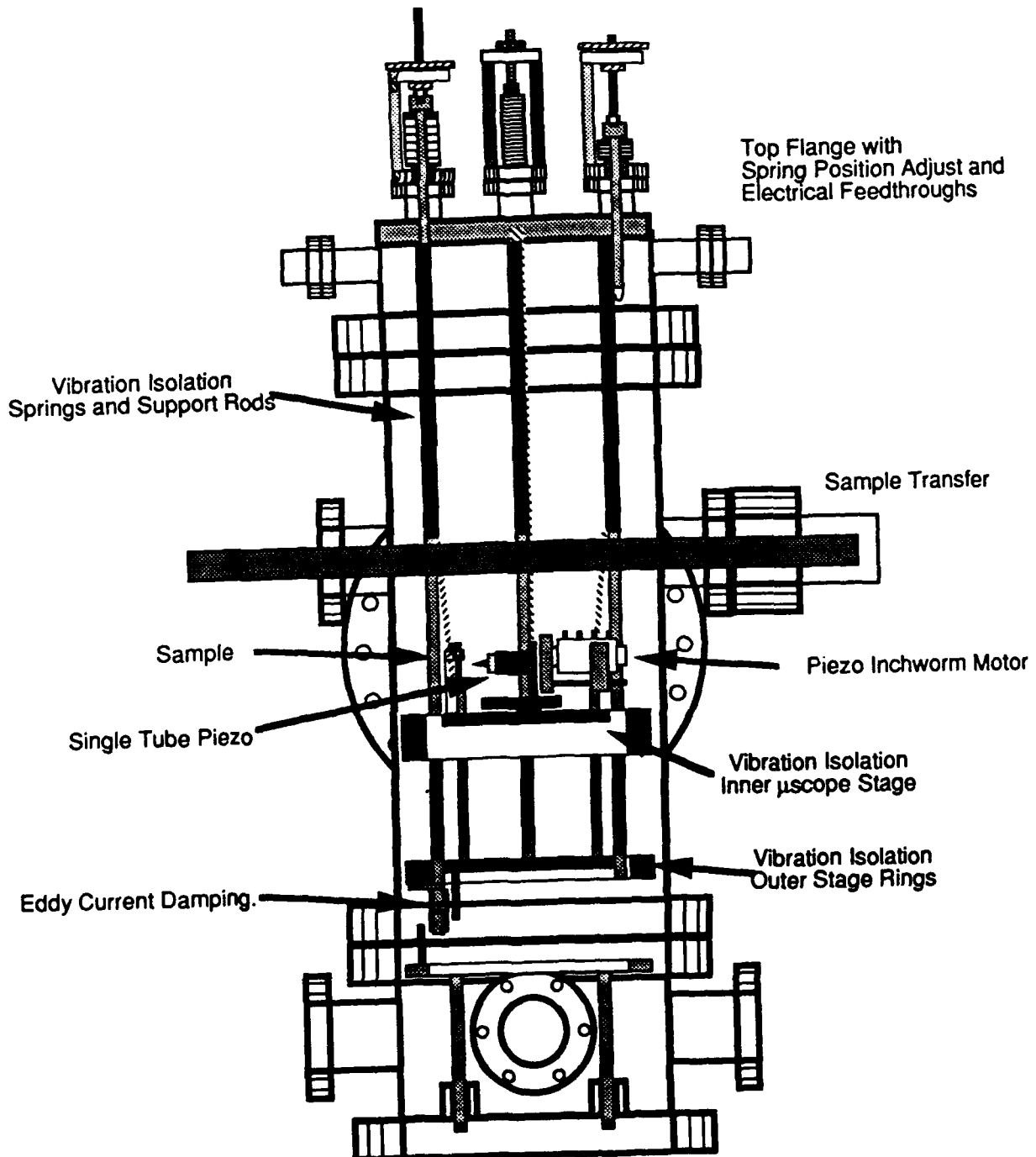
Microscope Chamber

Process/Analysis Chamber

Load Lock



New Version μ scope Side View



μ Scope Overview Top

